iScience

CellPress
OPEN ACCESS

Article

Stepwise remodeling and subcompartment formation in individual vesicles by three ESCRT-III proteins

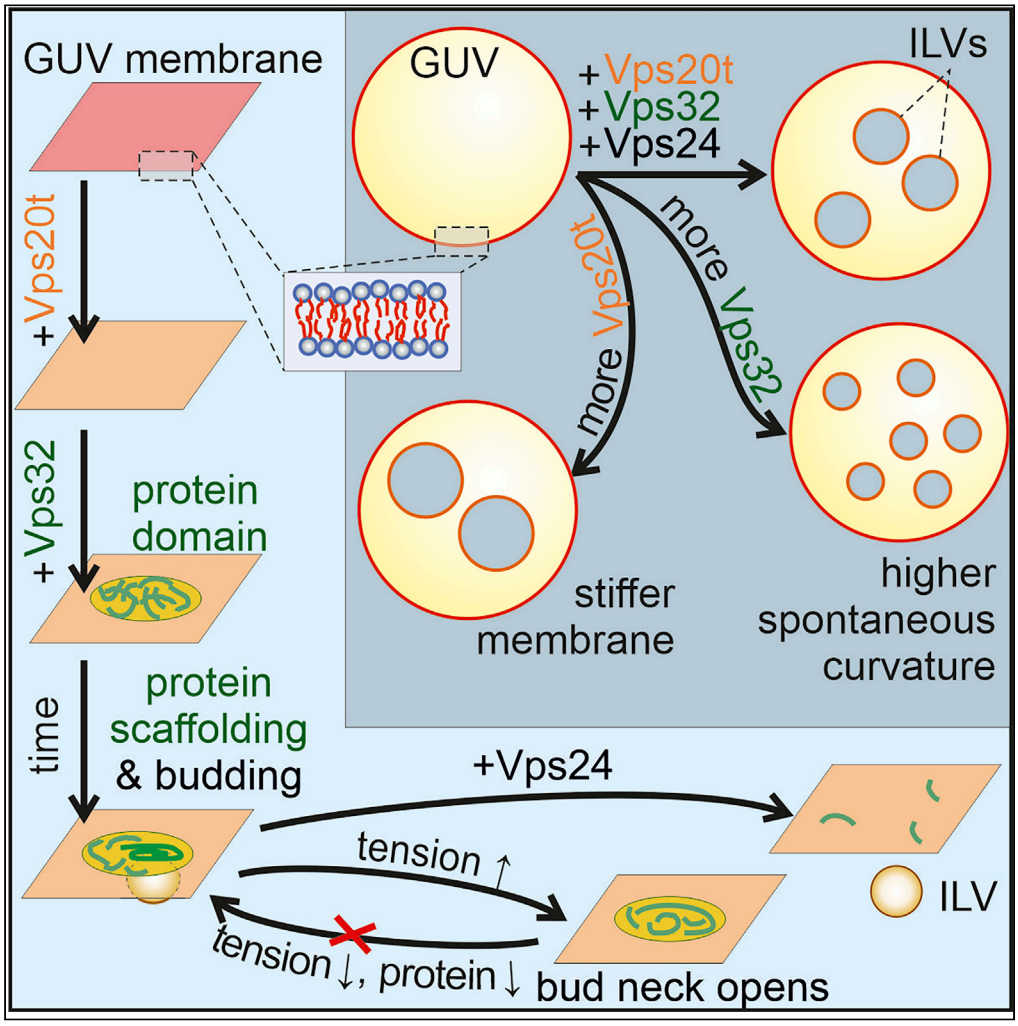

Yunuen Avalos-Padilla, Vasil N. Georgiev, Eleanor Ewins, Tom Robinson, Esther Orozco, Reinhard Lipowsky, Rumiana Dimova

rumiana.dimova@mpikg.mpg.de

Highlights

ESCRT-III proteins change membrane stiffness and spontaneous curvature

These properties modulate the size of buds and intraluminal vesicles

Bud stability depends on protein concentration and membrane tension

The ESCRT-III forms domain-like protein-rich patches on membranes

Avalos-Padilla et al., iScience 26, 105765
January 20, 2023
https://doi.org/10.1016/j.isci.2022.105765

iScience

CellPress
OPEN ACCESS

Article

Stepwise remodeling and subcompartment formation in individual vesicles by three ESCRT-III proteins

Yunuen Avalos-Padilla,[1,2,3,5] Vasil N. Georgiev,[1,5] Eleanor Ewins,[1] Tom Robinson,[1] Esther Orozco,[4] Reinhard Lipowsky,[1] and Rumiana Dimova[1,6,*]

SUMMARY

The endosomal sorting complex required for transport (ESCRT) is a multi-protein machinery involved in several membrane remodeling processes. Different approaches have been used to resolve how ESCRT proteins scission membranes. However, the underlying mechanisms generating membrane deformations are still a matter of debate. Here, giant unilamellar vesicles, microfluidic technology, and micropipette aspiration are combined to continuously follow the ESCRT-III-mediated membrane remodeling on the single-vesicle level for the first time. With this approach, we identify different mechanisms by which a minimal set of three ESCRT-III proteins from *Entamoeba histolytica* reshape the membrane. These proteins modulate the membrane stiffness and spontaneous curvature to regulate bud size and generate intraluminal vesicles even in the absence of ATP. We demonstrate that the bud stability depends on the protein concentration and membrane tension. The approaches introduced here should open the road to diverse applications in synthetic biology for establishing artificial cells with several membrane compartments.

INTRODUCTION

The endosomal sorting complex required for transport (ESCRT) was first described as a vacuolar protein sorting machinery in yeast.[1–3] Over the years, it has been demonstrated that the ESCRT machinery participates during membrane fission and remodeling in different processes including the formation of multivesicular bodies,[4] virus budding,[5] neuron pruning,[6] plasma membrane repair,[7,8] and autophagy[9,10] as reviewed in.[11–14] The ESCRT machinery is a multi-protein system formed by the sub-complexes ESCRT-0, ESCRT-I, ESCRT-II, ESCRT-III and a set of accessory proteins that act in a sequential manner to generate invaginations in the membrane.[15] Among these sub-complexes, ESCRT-III is the only protein family that remodels the membrane shape and it is also the most conserved across the eukaryotic lineage. Moreover, some members of the ESCRT-III family have been found in the Archaea taxa suggesting its ancestral function as a scission machinery.[16] The ESCRT-III complex is formed by Snf7-domain-containing proteins and the number of components varies among the different supergroups within the eukaryotic taxa, probably because of specialized evolution in the diverse organisms. The most essential proteins of ESCRT-III are Vps2, Vps20, Vps24 and Snf7/Vps32. All of them share a common structural core motif formed by at least four alpha helices with a positive net charge (core domain) with the propensity to bind to negatively charged lipid membranes.[17,18] ESCRT-III proteins also possess a negatively charged fifth alpha helix that blocks the core domain, thus, allowing the proteins to remain soluble in the cytoplasm in the absence of activating factors.[19,20]

Although membrane fission conducted by ESCRT-III is not fully understood, it is generally believed that ESCRT-III polymers bind transiently to highly curved regions of membranes,[21,22] and grow toward zones with less curvature.[23] The constriction of the bud neck is mediated by the formation of Vps32 polymers, later remodeled by Vps24, Vps2[24] and the ATPase Vps4[25,26] to produce domes and cones.[27,28] Theoretical estimates suggest that the formation of cones is more favored because it requires less adhesive strength of the protein-membrane interaction and is associated with higher constriction forces.[29]

Giant unilamellar vesicles (GUVs)[30,31] represent a well-established tool not only for elucidating membrane properties and remodeling,[30,32–34] but also as biomimetic containers in synthetic biology.[35–40] Different

[1]Max Planck Institute of Colloids and Interfaces, Science Park Golm, 14476 Potsdam, Germany

[2]Nanomalaria Group, Institute for Bioengineering of Catalonia (IBEC), The Barcelona Institute of Science and Technology, Baldiri Reixac 10-12, ES-08028 Barcelona, Spain

[3]Barcelona Institute for Global Health (ISGlobal, Hospital Clínic-Universitat de Barcelona), Rosselló 149-153, ES-08036 Barcelona, Spain

[4]Departamento de Infectómica y Patogénesis Molecular, CINVESTAV IPN, 07360 Ciudad de México, México

[5]These authors contributed equally

[6]Lead contact

*Correspondence: rumiana.dimova@mpikg.mpg.de

https://doi.org/10.1016/j.isci.2022.105765

studies using GUVs and the purified components of the ESCRT machinery have suggested that ESCRT-III is able to induce invaginations in membranes without the requirement of the upstream ESCRT factors.[41–43] Using the GUV platform has allowed resolving the role of various factors involved in ESCRT-membrane interactions, e.g.. the role of tension on membrane remodeling,[44] the formation of a protein-based diffusion barrier at the invagination neck,[45] and the importance of correct membrane topology and Vps4 for scission.[46] Furthermore, GUV-based studies have revealed the role of membrane curvature affecting protein polymerisation,[35,47] the influence of protein crowding on ESCRT-membrane remodeling processes,[48] and the importance of membrane composition on regulating protein affinity and surface organization.[49,50] In addition, our group has shown that the core domain of the recombinant Vps20 from *Entamoeba histolytica*, EhVps20(1–173) (hereafter referred to as EhVps20t), can bind to the membrane of GUVs, and together with EhVps32 and EhVps24 they are sufficient to generate vesicular subcompartments (which we will refer to as intraluminal vesicles, ILVs) in the same GUV.[41] Moreover, by using the same system, we have observed that alterations to the order of protein addition showed no significant differences but omission of any of them resulted in no ILV formation.[41]

Despite these findings, the factors governing the size of the intraluminal vesicles and the role of the membrane material properties in regulating the ESCRT-III activity are unknown. Indeed, knowing these factors should be useful to construct cell-size vesicles with nested compartments for the reconstitution of the structural mimicry of eukaryotes and their membrane-bound organelles. Such synthetic compartmentalization offers a route toward uncoupling enzymatic reactions or separating reagents. Although efforts in this direction have been already made, see e.g.,[51–54] the most successful case, allowing for control on the compartment size and number, relies on the implementation of microfluidics on double emulsions for the preparation of vesicles-in-vesicle (vesosome) systems.[51] The drawback of this approach, in which the vesicles are constructed in a layer-by-layer fashion, has certain disadvantages for protein reconstitution. We speculate that closer-to-nature generation of internal micron-sized compartments as those triggered by ESCRTs and regulating their properties via modulating determinants such as membrane composition and rigidity will pave the road toward more natural routes for creating synthetic cells with multiple compartments.

In the present study, we combined cellular and synthetic biology approaches to elucidate the mechanism for membrane budding and fission triggered by a minimal set of three ESCRT-III proteins from the highly phagocytic parasite *E. histolytica*. Using a single-vesicle assay, we identify three main steps of the membrane reshaping process: the first ESCRT-III component binds to the membrane, the second component binds to the first one and generates inward pointing buds, and the third one leads to membrane fission even in the absence of ATP (suggesting that cells can take advantage of passive processes). We demonstrate that the size of the generated ILVs does not depend exclusively on the size of the engulfed cargo, as previously suggested,[42] but is also influenced by the membrane mechanical properties and the protein coverage. The stability and reversible formation of intraluminal invaginations was probed against increased membrane tension employing osmotic inflation/deflation and micropipette aspiration of giant vesicles. The system described here offers a minimalistic approach for establishing a synthetic microcompartmentalized cell, in which the size and content of the compartments can be externally controlled.

RESULTS

Fission triggered by ESCRT-III proteins can be divided in three consecutive steps: Protein binding, membrane budding and fission

Previous studies[41,43,44,46] have investigated the simultaneous action of protein mixtures on GUV morphology, thereby probing the membrane response averaged over a batch of vesicles. This averaging procedure does not allow several important aspects of the membrane remodeling process to be addressed: Did the addition of one of the proteins compromise the membranes in terms of vesicle leakage and permeation? What was the initial morphology of the GUVs before they started to interact with the proteins? Indeed, vesicles in the same batch also have different membrane tensions typically in the range between 10^{-9} and 10^{-4} N/m and exhibit various morphologies depending on the leaflet asymmetry across the bilayer membrane[55] (they may even vary in composition when the membrane contains several molecular components[56,57]). Thus, we investigated the action of proteins on the same individual vesicle by adding them consecutively to this vesicle. To avoid possible effects of unbound proteins, a microfluidic device, which allows capture of GUVs and exchange of their external solution, was used to follow the interactions on individual vesicles.[58] GUVs composed of POPC:POPS:Chol:PI(3)P

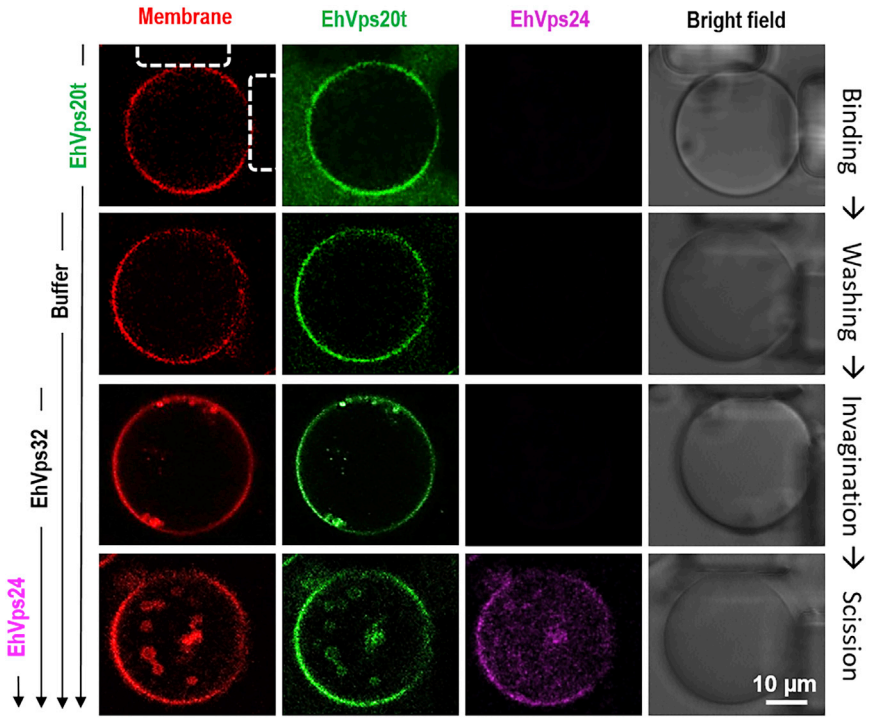

Figure 1. Single-vesicle assay for imaging the successive binding of ESCRT-III proteins, membrane (inward) budding and scission

Vesicles prepared from POPC:POPS:Chol:PI(3)P (62:10:25:3) and labeled with 0.1 mol % TR-DHPE were loaded on a microfluidic chamber at a flow rate of 10 µL/min. Then, 125 nM of EhVps20t (20% of the protein was labeled with Oregon green), 600 nM EhVps32 and 300 nM EhVps24 (20% of the protein was labeled with Alexa 633) were successively flushed in at a constant rate of 0.1 µL/min. Before introducing the next protein solution, the chamber was flushed with 100 µL of protein-free buffer to remove unbound proteins in the bulk as illustrated for EhVps20t with the first two rows of images. The snapshots show confocal cross sections and phase-contrast images (last column) of the same trapped vesicle after the flushing steps. Three main events are distinguished: EhVps20t binding of the membrane (first two rows), budding triggered by EhVps32 (third row) and scission directed by EhVps24 (last row). To avoid cross talk, the confocal images were obtained from sequential scanning. The microposts trapping the vesicle are seen in the last column of images and are indicated by dashed lines in the upper left image. Experiments were conducted three times and, in each experiment, at least two different vesicles were monitored for the whole sequence of flushing/incubation steps (see also Videos S1 and S2).

(62:10:25:3), roughly mimicking the endosomal membrane composition[59,60] and labeled with TR-DHPE were electroformed and captured between the posts in a microfluidic device; for details, see Figure S1 in the supporting information (SI). Thereafter, the three ESCRT-III components EhVps20t, EhVps32 and EhVps24 were sequentially flushed in at a constant flow rate of 0.1 µL/min. A total of 100 µL solution was used to obtain complete exchange at each solution-exchange step to ensure concentration control. After introducing each protein, the solution in the chamber was exchanged with the protein-free buffer (25 mM Tris, 150 mM NaCl, pH = 7.4) to remove the unbound proteins in the surrounding solution. This step aimed at resolving curvature effects specific to the particular protein added. Fluorescent analogues of EhVps20t and EhVps24 were used to monitor protein binding. Consistent with previous bulk studies on vesicle populations,[41] EhVps20t was observed to bind to the membrane of the GUVs. Even after a thorough washing, EhVps20t remains bound to the vesicle (Figure 1, first two rows of images). Note that close contact to the PDMS posts decreases the fluorescence signal from the membrane as previously observed.[61] After the addition of EhVps32 and slight deflation of less than 5% to allow for excess area, small invaginations (intraluminal buds) attached to the membrane of GUVs with relatively uniform size were observed (Figure 1, third row, Video S1 in the SI); similar deflation in the presence of EhVps20t was not found to result in detectable morphological changes in the GUVs (Figure 1, second row). Finally, the addition of ATP-free solution of EhVps24 triggered the scission of the newly formed ILVs and their release in the vesicle interior (Figure 1, bottom row). It was difficult to detect the ILVs from bright-field observations during the experiment because of spinning of the vesicles in the microfluidic flow. However,

the generated ILVs could be observed on refocusing and stopping the flow (Video S2 in the supplemental information). In this way, the ILVs were found to have a relatively homogeneous size distribution (1 ± 0.18 μm diameter, obtained by three independent replicas where 2 vesicles were followed) and were similar in diameter to the intraluminal buds generated after introducing EhVps32. Unlike ILVs, the size of intraluminal buds could not be measured systematically because of imaging artifacts arising from the proximity of the mother vesicle membrane. but we were able to estimate their sizes from those favorable cases for which the buds are clearly visible. Incubation of GUVs with six rounds of alternating buffer flushing and incubation, resulted in no ILV formation (Figure S2), indicating that the effect is due to protein activity and not because of buffer or flow in the microfluidic chamber.

Quantifying the amount of EhVps20t bound to the membrane: Dependence on protein bulk concentration

As shown previously, the interactions between ESCRT-III proteins and membranes are mostly mediated by electrostatic forces between positive residues and negatively charged lipids.[2,18,28,50] Despite the selective binding of upstream ESCRT factors to the endosomal enriched lipid PI(3)P,[62] several studies demonstrated that ESCRT-III proteins are able to bind to other negatively charged lipids. In particular, the binding and function of ESCRT-III proteins is not significantly different when using membrane compositions of PC:PS:Chol:PI(3)P and PC:PS with the same negative surface charge density,[9,41,63] as previously confirmed for *E. histolytica* ESCRT-III proteins.[64] For quantifying the amount of EhVps20t on the membrane, we used GUVs with a simpler lipid composition, namely POPC:POPS (80:20), which have a similar surface charge density as vesicle membranes made of POPC:POPS:Chol:PI(3)P (62:10:25:3).

To quantify the EhVps20t coverage, we analyzed the fluorescence signal from the labeled protein and extrapolated the concentration from a calibration curve obtained for a lipid labeled with the same fluorophore, namely the Oregon green 488 labeled lipid OG-DHPE; an approach reported earlier for assessing concentrations of self-penetrating peptides at membranes.[65] The fluorescence signal in the membrane, I, measured at different pre-set molar fractions of OG-DHPE in the vesicles (Figure 2A, see Figures S3–S5) was found to follow the linear dependence: $I \cong 115 n_{OG} - 7$ [a.u.], where n_{OG} is the mole fraction (in %) of OG label in the membrane. Then, the intensity signal from protein labeled with the same fluorescent group, OG-EhVps20t, and bound to the outer leaflet of the vesicle membrane was measured and the background signal from free protein in the bulk subtracted (see Figure S5). The molar fraction of the protein at the membrane of vesicles made of POPC:POPS (80:20) was determined using the calibration curve (taking into account that the fluorescence from the protein at the outer vesicle leaflet should be compared to half the intensity of OG-DHPE located in both leaflets). Finally, the possible difference in the quantum yield of the fluorophore (OG) labeling the lipid and the protein was also accounted for from intensity measurements of solutions of labeled lipid solutions and of the labeled protein (see STAR Methods and Figure S6A). The EhVps20t coverage was plotted as protein per membrane area (Figure 2B). For this, we considered the membrane of simpler compositions and took into account that the area per lipid molecule is 0.68 nm^2 for POPC[66] and 0.55 nm^2 for POPS[67]; we assumed that the molecular areas are preserved in the mixed membrane. The ratio of labeled to unlabeled protein in the experiments (1:4) was also considered. The protein coverage on vesicles prepared from POPC:POPS:Chol:PI(3)P (62:10:25:3) was found to be similar as expected from the comparable surface charge, see Figure S6B.

The results in Figure 2B show a Langmuir-type adsorption isotherm where the membrane coverage of EhVps20t increased with protein bulk concentration and reached saturation at around 800 nM (Figure 2B) protein in the bulk. From the obtained membrane coverage of the protein we could roughly assess the area a single molecule EhVps20t occupies at the membrane. Our approximate estimates show that the area containing a single protein molecule decreased with increasing bulk concentration of EhVps20t. For instance, the available membrane area per single protein molecule of ~67 × 67 nm^2 at 125 nM of EhVps20t decreased to ~48 × 48 nm^2 for the highest coverage (at 800 nM EhVps20t); see Figure 2C. For comparison, the dimensions of the protein predicted from the crystal structure of other ESCRT-III homologues are 39.2 × 33.7 × 96.4 $Å^3$ (following modeling reported in[41]), but the activated protein (with open conformation) has a larger size[18] and could prevent further protein binding by electrostatic interactions. Note that the obtained areas per single protein correspond to conditions far below surface concentrations of proteins observed to trigger curvature generation and fission because of crowding.[68] Only at the highest explored concentration (1200 nM EhVps20t) were the vesicles occasionally observed to exhibit outward tubulation potentially indicating steric interactions and tendency to generate positive curvature; see inset in Figure 2B.

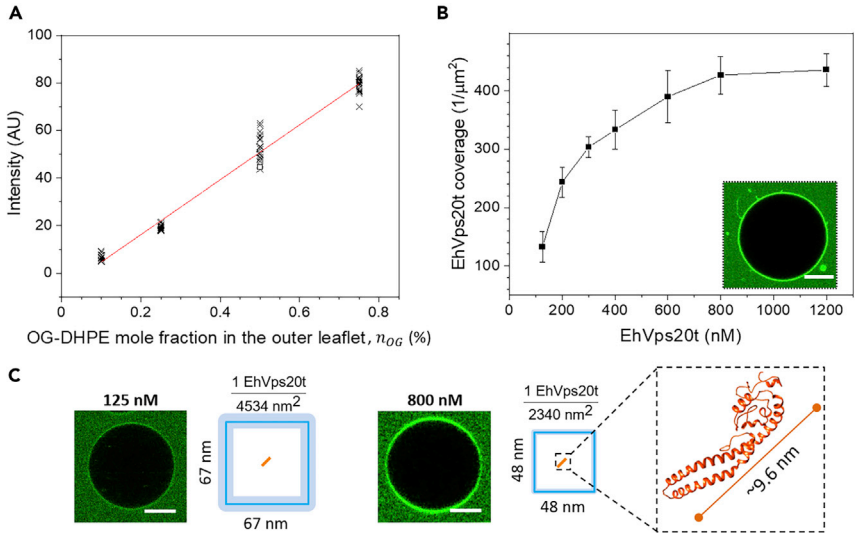

Figure 2. Quantitative measurement of EhVps20t bound to the membrane

(A) Calibration curve of the average intensity per pixel obtained with different concentrations of OG-DHPE in POPC:POPS (80:20) GUVs equilibrated in protein buffer (25 mM Tris, 150 mM NaCl, pH = 7.4). The symbols represent measurements on different vesicles and the red line is a linear fit (see text for expression).

(B) Quantitative estimate for the coverage of EhVps20t (number of protein molecules per membrane area) for different bulk protein concentration at which POPC:POPS:Chol:PI(3)P (62:10:25:3) GUVs were incubated. In each condition, triplicate incubations were done. Symbols represent the mean value and vertical lines the standard error of the coverage measured on 20 GUVs. The insert shows outward tubulation observed when 1200 nM of EhVps20t was used.

(C) Representative images of the coverage of EhVps20 t at the membrane for two different concentrations (125 nM and 800 nM), both of which are dilute and small compared to conditions of protein crowding. The depicted fractions and squares indicate the average areas occupied by a single molecule of EhVps20t (orange line, in scale with the square size; the thickness of the light blue square border illustrates the error) in the respective conditions. The predicted 3D structure and approximate size of EhVps20t in crystalline state is also given (note that upon binding the protein could unfold and occupy a larger area). Scale bars: 20 μm

Stability and remodeling of intraluminal buds

Next, we aimed to explore the stability and remodeling of the intraluminal buds and how they can be affected by alterations in membrane tension and on removal of the protein excess. Tension was modulated using two approaches: (1) Osmotic inflation and (2) micropipette aspiration. For both approaches, electroformed GUVs from the lipid mixture of POPC:POPS:Chol:PI(3)P (62:10:25:3) were incubated with 125 nM EhVps20t and 600 nM EhVps32 (mixture 1) and observed by confocal microscopy. As expected, spherical buds appeared (Figures 3A–3C, top row of images).

Osmotic inflation

For this approach, the mixture of proteins and GUVs (mixture 1) was diluted 1:2 with a hypotonic solution (of 20% lower osmolarity) to inflate the vesicles, see STAR Methods. After inflation, we observed that the previously formed intraluminal buds disappeared, implying that the bud necks could be opened by increasing the membrane tension (Figure 3A, inflation). We then performed a mild deflation step of 10% osmolarity increase. In this case, we detected the formation of buds and long necklaces of small spheres with a typical size of 1–2 μm, Figure 3A, deflation (see also Video S3). Note that a constant concentration of proteins was maintained throughout the whole experiment; in the absence of proteins or when the total amount was diluted, such necklace-like structures were not observed on deflation.

In these bulk experiments, the initial state of the observed vesicles (and. in particular, whether the vesicle had internal/external structures before the inflation/deflation steps) is not known. To overcome this uncertainty, microfluidic devices were used to follow the same vesicle exposed to inflation and deflation, thus eliminating effect of pre-existing buds formed during growth, harvesting and mixing. In this approach, the unbound proteins are removed and some bound proteins may also be washed away (note that experiments with constant concentration of proteins was not feasible in this case because

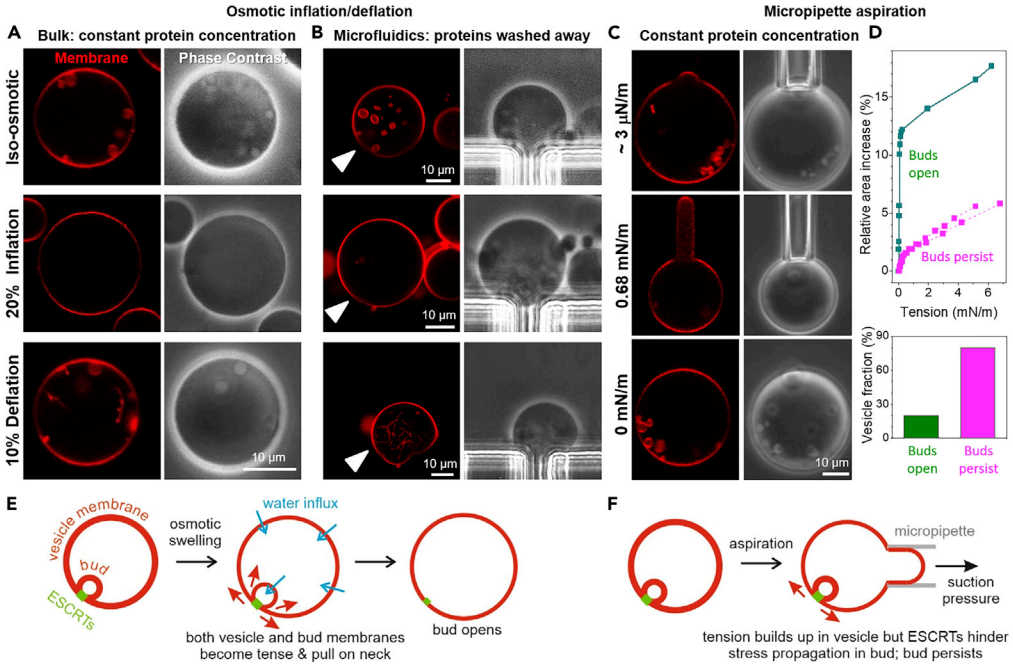

Figure 3. Stability and remodeling of intraluminal buds upon variations in membrane tension imposed by osmotic inflation/deflation and by micropipette aspiration of GUVs in the presence of EhVps20t and EhVps32 only

(A–C) Electroformed POPC:POPS:Chol:PI(3)P (62:10:25:3) GUVs were incubated with 125 nM EhVps20t and 600 nM EhVps32 and (A) observed in bulk, (B) loaded in a microfluidic chamber or (C) aspirated in a micropipette. In all cases, intraluminal buds were observed (see first row and zoomed inset). Afterward, (A and B) the GUVs were incubated with a hypotonic solution to inflate them up to 20% which led to bud suppression. Increase in the suction pressure in the micropipette (C and D) only occasionally (in 20% of the vesicles) led to opening of the membrane neck connecting the bud to the mother vesicle. Note that while (A) shows different GUVs, in (B) and (C) we follow the same vesicle during the experimental steps (arrowheads point to the monitored vesicle, which was thoroughly examined also with 3 days confocal scans). Then, a mild deflation (10%; a and b) and pressure release (c) were applied (last row of images). In the bulk experiment (A) where the total protein concentration was kept constant, we observed the formation of necklaces of small spheres (see also Video S3), whereas in the microfluidic device (B), where the free proteins were washed away, tubes with sub-microscopic diameters were observed after the deflation step (see Video S4). In aspirated vesicles where buds open, they reform on suction pressure release

(D) The majority of aspirated vesicles (n = 15) do not show bud opening even when the tension is increased up to about 6 mN/m above which the vesicles rupture. Three examples for area-tension traces are shown.

(E) During osmotic inflation, water permeates across the membranes of both the mother vesicle and the bud, increasing the tension in both membranes (two pairs of red arrows); both compartments are drawn with thinner contours to reflect the higher tension of their membranes; indeed, in the high-tension regime of stretching, the membrane should become thinner). This leads to opening of the bud neck.

(F) On the other hand, by micropipette aspiration only the membrane tension in the mother vesicle (only one pair of red arrows) is directly increased; only the vesicle membrane becomes tense as reflected by the thinner contour, but not that of the bud. Stress propagation to the bud membrane is plausibly hindered by the ESCRT proteins assembly stabilizing the bud neck

of the high protein amounts required). GUVs (mixture 1) were loaded in a microfluidic chamber. The trapped vesicles typically exhibit a smaller number of buds than those in bulk measurements because the posts of the traps provide additional constraints on the trapped vesicles reducing the excess area available for budding (note that on stopping the flow, the deformation from the posts is absent but budding is preserved). After a 20% inflation step, the GUV volume increased and the buds disappeared (Figure 3B, inflation), similarly to the behavior of the vesicles under bulk dilution (Figure 3A, inflation). However, on 10% deflation, the vesicles did not develop micron-sized buds but only inward tubes with sub-optical diameters (Figure 3B, deflation; see also Video S4) presumably resulting from the solution asymmetry. This suggests that in the bulk experiment (Figure 3A), where the proteins are still present (contrary to the case of deflation in the microfluidics experiment as in Figure 3B), the newly formed buds and necklaces, whose micron-sized buds are comparable in diameter to those of the intraluminal buds, are

stabilized by newly bound proteins available in the external solution (but absent in the microfluidics experiment). The stability of single buds versus interconnected necklace multi-buds depends on membrane spontaneous curvature,[69–71] here governed by the proteins; both single buds and necklaces can be formed for the same shape parameters, i.e., for the same spontaneous curvature and vesicle volume-to-area ratio, see,[69] but the kinetics and dynamics of these parameters likely determine the stable shape. Note that studies in worms[72] and in plants[73] showed similar buds interconnected into necklaces (concatenated structures) forming under the influence of ESCRTs.

In both, bulk and microfluidics experiments, the intraluminal buds are suppressed by osmotic inflation (they open up as a result of built-up membrane tension) and do not reform to the same extent on tension release (deflation) suggesting irreversible remodeling of the scaffold-like structure of polymerized protein. Even though the binding of EhVps32 to EhVps20t is relatively strong[74,75] depleting EhVps32 from the bulk could result in desorption of the protein. We thus speculate that in the microfluidic chamber, on increased tension and partial protein desorption, the EhVps32-protein scaffold irreversibly deforms failing to trigger the bud-like invagination when the membrane is deflated again. In contrast, in the bulk experiments, the free proteins in the bulk solution can bind triggering the formation of new inward structures with dimensions similar to the initially observed intraluminal buds.

Micropipette aspiration

As we mentioned above, adding proteins together in a mixture or in a step-by-step manner does not have any influence on the number of GUVs with ILVs (Figure S7). To isolate the effect of potentially desorbing proteins during the microfluidic inflation experiments, we probed the bud stability while keeping the protein concentration constant. For this we used micropipette aspiration, see STAR Methods. A small fraction of the vesicles showed bud opening (Figures 3C and 3D). One such example is shown in Figure 3C. The tension was gradually increased, and the buds opened at tensions slightly above 0.01 mN/m. After gradual decrease in the tension, the buds reformed. The majority of the aspirated GUVs (80%) did not exhibit bud opening even in the regime of high membrane tension up to around 6–7 mN/m, close to the lysis tension. Above this tension, the vesicles collapsed being sucked up inside the pipettes. When bud opening was observed during aspiration (20% of the vesicles), it occurred at tensions (0.01–0.1 mN/m) which are considerably higher than the spontaneous tension (generated by the spontaneous curvature arising from the protein adsorption), the upper limit of which is on the order of 4×10^{-5} mN/m as estimated from the intraluminal bud size, see ref.[70,76] Thus, protein assembly and scaffolding must be stabilizing the buds. For a radius R_{ne} of the membrane neck in the range between 5 and 25 nm, a tension of $\Sigma = 0.1$ mN/m at which neck opening was observed, implies the neck opening force $f \sim 2\pi R_{ne}\Sigma \sim 3 \div 16$ pN generated by the membrane tension. This argument however ignores the membrane tension in the bud membrane and assumes uniform curvature-elastic parameters, the validity of which is unclear.

Protein domains, and protein and lipid mobility in intraluminal buds

To check whether the assembly process of the two ESCRT proteins can be visualized in real time in the membrane of the GUVs, lower concentrations of the protein were used and the vesicles were monitored individually in the microfluidic device. For the protein concentrations discussed so far, we observe that budding has occurred in most vesicles already after less than 5 min (Figure S8A). At lower EhVps32 protein concentrations, bud formation is slowed down. For instance, at 300 nM of EhVps32, maintaining EhVps20t concentration at 125 nM, the budding is delayed by up to 15 min after protein addition. Furthermore, when we increased the concentration of EhVps32 to 750 nM, the budding process started already 1 min after protein addition. In accordance with these observations, the number of buds gradually increases with the concentration of EhVps32 (see Figure S8). After 10 min incubation of GUVs with proteins at low concentration, namely 125 nM EhVps20t and 300 nM EhVps32, we were able to detect EhVps32-rich protein domains in the membrane by monitoring the fluorescently labeled analogue OG-EhVps32 (top row in Figure 4A, arrow). It is important to note that in the presence of EhVps24 we did not detect protein domain formation (probably because of the high protein concentration or the enhancing activity of EhVsp24 that changes EhVps32 filaments conformation, while speeding up the process), suggesting a regulatory role of this protein. Of interest, EhVps32-rich domains appeared to differ in their lipid composition as well, as concluded from the enhanced intensity of the membrane dye $DiIC_{18}$ (top row in Figure 4A). We speculate that these domains represent accumulation of membrane folds with sub-optical resolution dimensions, because no thickening of the vesicle membrane was

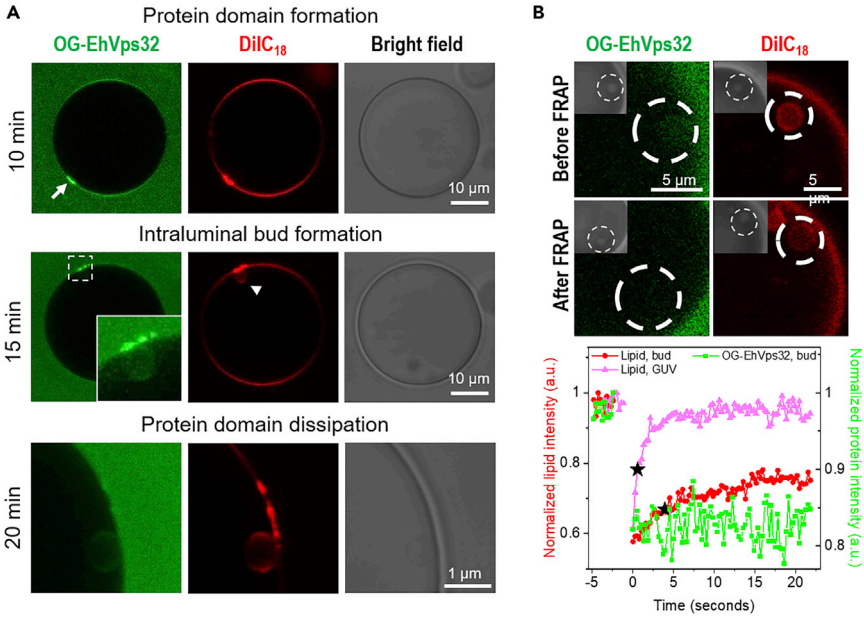

Figure 4. EhVps32–enriched domain formation and protein and lipid mobility in intraluminal buds

GUVs composed of POPC:POPS:Chol:PI(3)P (62:10:25:3) and loaded in a microfluidic device were incubated with 125 nM of EhVps20t and 300 nM of EhVps32 (20% of EhVps32 was labeled; both proteins are added at the same time).

(A) Images of the same GUV taken after incubation of 10, 15 and 20 min (inset and last row showing the zoomed region of the same intraluminal bud) respectively showing the formed protein-enriched domain, the formation of intraluminal bud and protein domain disassembly. Images correspond to a representative image of at least 30 vesicles observed.

(B) FRAP measurements made on an intraluminal bud formed on a different vesicle, of which only a zoomed segment is shown with the bleached region indicated by the dashed circles. The images show protein and lipid fluorescence from the region of the intraluminal bud before (top row) and after (bottom) bleaching; inserts display the phase-contrast image clearly showing the location of the bleached intraluminal bud. The curves below (collected consecutively) demonstrate the lack of fluorescence recovery of the protein signal (green) and partial recovery of the lipids in the bleached intraluminal bud (red); the pink curve represents lipid recovery signal in a region at the vesicle surface. The black stars indicate the half-time of the lipid fluorescence recovery, which is 0.57 and 3.87s for the vesicle surface and the intraluminal bud, respectively.

detected under phase contrast (top and middle row in Figure 4A). Fifteen to 20 min after the incubation (throughout which the vesicle and the domain were constantly monitored), membrane invagination and budding occurred at the site where the protein domain was formed (middle row in Figure 4A, arrowhead, Figure S9). The formation of the intraluminal bud was associated with partial to complete dissolution of the EhVps32-rich domain (bottom row in Figure 4A). Presumably, the accumulated protein rearranged while scaffolding the inward bud. Note that the signal from the domain-segregated lipids (red channel in bottom row of Figure 4A) did not fully decay even after the formation of the intraluminal bud suggesting mild membrane remodeling by remnant protein. In any case, EhVps32 domains were detected also in unlabeled GUVs (Figure S9), suggesting that their formation is mediated mainly by this protein.

To resolve whether the protein remained locally immobilized at the membrane of the intraluminal bud indicating a rigid assembly, we examined the recovery of fluorescence signal from OG-EhVps32 after photobleaching. The FRAP experiments (Figure 4B) did not indicate recovery of the OG-EhVps32 signal after bud bleaching suggesting that the assembled proteins are immobilized. Note however that the initial signal in the bud is generated both from bound and unbound protein, which cannot be distinguished. We thus conclude that EhVps32 is locally immobilized and is not able to pass through the narrow neck of the bud nor is additional protein from the mother vesicle able to diffuse through the neck (only a limited amount of lipid does). In contrast, after photobleaching the same intraluminal bud, the lipid fluorescence partially recovered (contrary to observations for the human Vps2 protein, CHMP2B, which was reported to prevent lipid diffusion[45]). It is worth noting that full recovery was observed when photobleaching a region of the lipid membrane in the top area of the GUV (Figure 4B), with a lipid diffusion coefficient 5.8 µm/s which

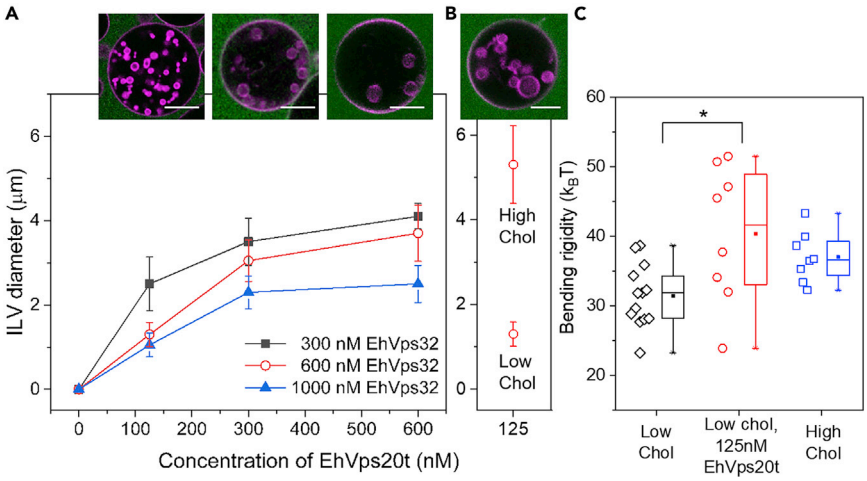

Figure 5. Antagonistic effects of EhVps20t and EhVps32 on the size of ILVs and role of cholesterol content in the membrane

(A) The ILV size was measured on GUVs made of POPC:POPS:Chol:PI(3)P (62:10:25:3) in protein buffer (25 mM Tris, 150 mM NaCl, pH = 7.4). Three different concentrations of EhVps20t (125, 300 and 600 nM) were tested in combination with three concentrations of EhVps32 (300 nM in black, 600 nM in red and 1000 nM in blue). All proteins were added at the same time. The statistical analysis of the data for significant difference is given in Table S1.

(B) For high-cholesterol fractions in the membrane, GUVs made of POPC:POPS:Chol:PI(3)P (52:10:35:3) were used. In all conditions (a, b), the concentration of EhVps24 was maintained at 200 nM. Proteins were added simultaneously to the vesicle suspension and the vesicles monitored in a microfluidic chip. The diameter of ILVs generated in all possible combinations, was measured and plotted against the concentration of proteins. Experiments were performed by triplicate and in each condition 20 GUVs with at least four ILVs were measured. The data represent the mean and the SE. The confocal sections on top display representative images of the red open-circle data in panel (A) and high-cholesterol composition in panel (B); in here, 20% of labeled EhVps20t (green) was used to follow the effect on the membrane (magenta). Scale bars: 10 μm.

(C) The bending rigidity of the membranes with low and high cholesterol fractions, POPC:POPS:Chol:PI(3)P (62:10:25:3) and (52:10:35:3) respectively, was measured from fluctuation spectroscopy of GUVs prepared in 20 mM sucrose and diluted in isotonic glucose solution with or without EhVps20t (125 nM). The measurements (see STAR Methods) were conducted at room temperature (~23 °C). The data points on the left of each bar show the individual measurements on different vesicles (at least 8 vesicles per composition were examined). Mean values and standard deviations are also given.

is comparable to literature data. Presumably, the EhVps32 scaffold impedes the lipid mobility within the membrane of the bud.

Membrane remodeling by EhVps20t and EhVps32 is antagonistic

Next, we aimed at understanding the mechanisms controlling the size of the generated buds. Precise imaging and size determination of buds is hindered by the vicinity of the mother GUV membrane. We thus assessed the sizes of ILVs. They were measured at 125, 300 and 600 nM concentrations of EhVps20t. Each EhVps20t condition was tested in combination with three different EhVps32 concentrations, arbitrarily named low, medium and high (300, 600 and 1000 nM respectively), all in the presence of 200 nM EhVps24 necessary for membrane scission. All proteins were added simultaneously to the vesicle suspension. Solution osmolarities were carefully adjusted along the experiment; note that incubation with protein-free buffers led only to the vesicle deflation but no formation in micron-sized buds/ILVs. Based on previous work,[41,43] EhVps32 concentrations lower than 300 nM were not sufficient to generate ILVs in giant vesicles, and concentrations higher than 1.3 μM induced GUV disruption (presumably resulting from high steric surface pressure as observed with other proteins[68]). All possible combinations of both protein concentrations were tested and the size of the ILVs was measured from 3D confocal scans. The diameter of the ILVs was found to increase with EhVps20t concentration in the batch (Figure 5A), presumably because of membrane stiffening. On the contrary, EhVps32 appeared to stipulate higher curvature resulting in smaller size of the ILVs with increasing protein concentrations (Figure 5A). Taken together, these results suggest that the two proteins act antagonistically and that at least two different mechanisms influence the curvature of the membrane and therefore, the size of the generated ILVs.

The size of ILVs is controlled by competing mechanisms of curvature generation and regulation

In the following, we attempted to disentangle the contribution of the ESCRT-III proteins in regulating the size of the ILVs. We considered only the effect of EhVps20t and EhVps32 as EhVps24 appears to induce the scission of vesicles from formed intraluminal buds with already defined diameter. Previous work demonstrated that EhVps32 and its activated version, EhVps32(1–165) do not bind to the membrane of negatively charged GUVs and do not produce ILVs in the absence of EhVps20t.[41] Therefore, EhVps32 by itself is unable to generate significant changes in the bare membrane of GUVs with endosomal composition when compared to incubation with buffer only. As observed in the above experiments, increasing the concentration of EhVps20t added to GUVs, increased the size of the generated ILVs, whereas the opposite effect was observed with EhVps32, see Figure 5A, with trends suggesting that EhVps32 builds its effect on the EhVps20t-coated membrane.

To distinguish the effects of the two proteins and their bending energy contributions, we first probed whether the bending rigidity of the GUVs is altered by the adsorbed EhVps20t. For this, we performed fluctuation spectroscopy[77,78] of vesicles in sugar solutions (see STAR Methods); the coverage of EhVps20t on the membrane in these conditions was found to be the same as that in the salt buffer (Figure S6). Note that measurements in the presence of EhVps32 were not feasible because the formed inward buds suppressed the fluctuations. The bending rigidity of protein-free GUVs (31.5 $\pm$ 4.5 k_BT; this value is relatively high compared to that of fluid neutral membranes but consistent with increased stiffness observed for membranes with higher charge density[79]) was found to increase (to 40.4 $\pm$ 10.0 k_BT) when 125 nM of EhVps20t was introduced (Figure 5C). Here, k_BT is the thermal energy at room temperature. The observed stiffening cannot be caused by protein myristoylation because EhVps20 lacks the glycine residue in its N-terminal (see Figure S10), which would be necessary for the myristolylation process. Higher protein concentrations (200 nM and higher) could not be explored because the shape fluctuations of the membrane were suppressed and could no longer be analyzed; we also observed "protein clusters" at the membrane of the GUVs (Figure S11), which are absent at high salinity. These clusters affected the detection of the vesicle contour for bending rigidity measurements. The membrane stiffness was found not to be influenced by the salinity buffer itself, Figure S12.

To find out whether the rigidity of the protein-free membrane can regulate the diameter of ILVs in the same way as EhVps20t does, we measured their size in GUVs with stiffer membranes of increased cholesterol fraction. Note that cholesterol is known to increase the bending rigidity of some[80] but not all membranes,[78,81,82] see overview in.[83] To confirm that we work with stiffer membranes, we measured the bending rigidity of the vesicles with low and high cholesterol fractions. As a high-cholesterol membrane, we explored vesicles made of POPC:POPS:Chol:PI(3)P (52:10:35:3), which compared to the standard mixture (62:10:25:3) preserves the surface charge (to ensure similar binding of the proteins) while increasing the cholesterol fraction by 10 mol %. The respective membrane bending rigidities for the high-cholesterol mixture and the standard mixture with low cholesterol content were found to be 37.0 $\pm$ 3.6 k_BT and 31.5 $\pm$ 4.5 k_BT (Figure 5C). Consistently, for the stiffer membrane, the ILV size was significantly larger, see Figure 5B, suggesting that it is modulated by changes in the membrane bending rigidity imposed by the adsorption of EhVps20t. Protein density variation affecting the ILV size in vesicles with different cholesterol fraction can be excluded as the protein coverage for both membranes was found similar (Figure S6). Note also that for much stiffer membranes made of DOPG:eSM:Chol 20:60:20 no intraluminal bud formation was detected, confirming that the stiffness of the bare membrane plays a significant role.

Changes in the membrane stiffness are correlated with changes in the spontaneous curvature which is reciprocal to the bending rigidity.[84,85] In homogeneous membranes, the magnitude of the spontaneous curvature is roughly inversely proportional to the bud size,[86] see also section 4 in[87] for a summary of approaches to assess the membrane spontaneous curvature. In our experiments, a decreased ILV size was observed when increasing the EhVps32 concentration (at a fixed EhVps20t concentration), suggesting the generation of more negative spontaneous curvature or the formation of a polymerized protein scaffold at the membrane. The overall impact of the two proteins on the membrane with endosomal composition is summarized in Figure 6A and discussed further below. The final ILV size is governed by a competition between the bending rigidity, increased by EhVps20t binding, and the spontaneous curvature enhanced by EhVps32 polymerization.

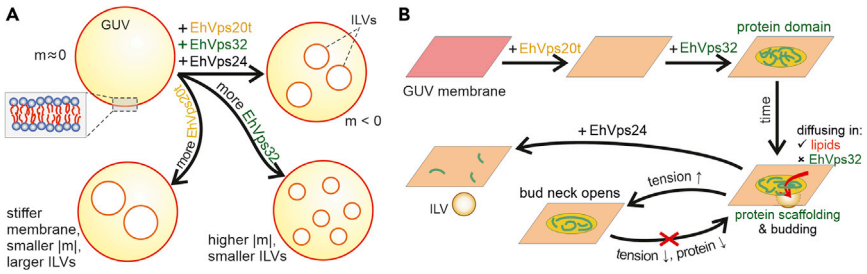

Figure 6. Schematic illustration and proposed scheme of the action of ESCRT-III proteins on membranes of endosomal mimetic

(A) EhVps20t and EhVps32 influence the spontaneous curvature, m, and bending rigidity of the GUV membrane, regulating the size of intraluminal vesicles. Increasing the concentration of EhVps20t leads to membrane stiffening and larger ILV size while raising the concentration of EhVps32 can enhance the membrane curvature while scaffolding the membrane into smaller ILVs.

(B) Proposed schematics of action. EhVps20t homogeneously binds to the membrane, whereas EhVps32 generates protein-rich domains. Over time, a nascent vesicle (intraluminal bud) is formed at the site of the domain. Protein diffusion through the neck is presumably blocked but lipids can still diffuse in the bud although to a limited extent. The bud neck can be open on tension increase, but releasing this tension does not allow for reforming this bud supposedly because of the irreversibly distorted protein assembly. Abscission of the intraluminal bud is mediated by EhVps24.

DISCUSSION

In general, fission implies a sequence of membrane deformation processes that finally lead to the formation of two independent membrane compartments from one. In some cases, fission is mediated by membrane protein coats or complexes and constriction (i.e., dynamin). In others, it is triggered by local membrane perturbation (i.e., by lysolipids and ENTH).[88,89] Recently, another mechanism has been discovered where molecular crowding seems to be sufficient to drive membrane scission as long as proteins bind to the membrane at a high coverage and their steric pressure overcomes the barrier for membrane scission.[68] Even at low protein concentrations, spontaneous curvature can generate forces sufficient to constrict and fission the membrane.[70,90] Until now and despite the effort, the precise mechanism by which the ESCRT machinery triggers membrane fission is not completely understood.

Over the past few years, several studies have reconstituted the action of the ESCRT-III machinery in GUVs.[28,35,41–44,46,91] In most of these experiments, purified ESCRT-III proteins were added to a batch of GUVs contained in a chamber and images were taken of different GUVs. The proteins remained in the batch throughout the whole reaction making it difficult to assign a specific task to each protein. In this study, using microfluidic technology we were able to trap GUVs and follow the ESCRT-induced remodeling on the same vesicle; multiple vesicles trapped at the microposts of the microfluidic device could be monitored (Figure S1). The main advantage of this approach is that unbound proteins are washed away before the addition of the next protein allowing a more controlled experiment and decoupling the distinct roles of the different proteins. In this way, we demonstrate that using a minimal system of only three ESCRT proteins and a microfluidic approach, we are able to establish a synthetic microcompartmentalized cell mimetic, in which the compartment size and its content can be controlled. The three-protein construct also offers a relatively simple approach for establishing synthetic cell division,[92] even in the absence of an energy source such as ATP.

Three main events during the ESCRT-III-mediated membrane remodeling have been identified and elucidated using a single-vesicle assay: binding of EhVps20t to the GUV membrane, invagination and budding of this membrane triggered by EhVps32, and membrane scission after EhVps24 addition (Figure 1), thereby mimicking the *in vivo* production of intraluminal vesicles with a minimal set of components. It is important to mention that the micrometer size of ILVs in our reconstitution experiments is significantly larger than that of ILVs observed in cells (~50 nm[93]). One possible reason as proposed previously[48] is the higher specific binding efficiency of ESCRT-III to the endosomal membrane compared to the GUV membrane as well as the absence of cargo proteins in the latter system. However, we did observe that the generated buds were homogeneous in size, which suggest that the size regulation is governed by factors such as protein surface coverage and membrane bending rigidity as demonstrated here (Figure 5).

It has been suggested that ESCRT-III is a dynamic polymer where multiple subunit turnover events trigger the deformation and scission of the membranes. In particular, Pfitzner et al.[94] demonstrated that the Vps32 polymer recruits the Vps2-Vps24 sub-complex, which in turn recruits Vps4. The enzyme promotes polymer growth and exchanges Vps24 for Did2, stimulating Vps4 activity, which leads to the disassembly of Vps32 and Vps24 filaments. Finally, the increasing levels of Did2 promote 3D deformation and intraluminal budding, after which Ist1 induces final scission.[94] In our model of GUVs system, we have found that EhVps4 was not necessary for the formation of ILVs. Protozoan parasites, including *E. histolytica* exhibit a substantial reduction of the ESCRT machinery compared to higher eukaryotes such as yeast and human. Indeed, ESCRT-III subunits in this parasite lack MIT-interacting motifs (MIM) which are responsible for the binding to microtubule-interacting and transport (MIT) domain of Vps4 in its human and yeast orthologue.[95] Therefore, we hypothesize that the mechanism of subunit turnover responsible for membrane remodeling and budding as well as ESCRT-III mediated scission *in vivo* could be occurring (at least in part) independently from EhVps4 as we show in our work.

To increase the understanding of the mechanisms that drive the membrane remodeling processes, we focused on investigating the first two steps (binding and invagination), which also define the size of intraluminal vesicles. We first measured the coverage of EhVps20t on the membrane of the GUVs (Figure 2) and observed saturation of the protein surface concentration at the membrane when the bulk protein concentration was about 800 nM. Presumably, EhVps20t acts as a nucleation point for the polymerization of EhVps32 as previously suggested,[96,97] therefore providing the specific surface area that would control the size of the generated ILV. Our estimates for the area occupied by EhVps20t (Figure 2C) agree with the diameters observed in deep-etch electron microscopy of plasma membranes from cultured cells depleted of Vps4 where ESCRT filamentous assemblies with diameters between 108 $\pm$ 30 nm were preserved.[98] We conclude that EhVps20t restricts the area available for EhVps32 polymerization and, therefore, ILV size regulation. From a synthetic point of view, ILVs represent microcompartments that are biomimetic analogues of cellular organelles and having control over their size and composition is advantageous. Obviously, the membrane coverage and bulk concentration of these two proteins could provide control parameters for organelle size in artificial cells, at least in the range 1–6 μm as shown in Figures 5A and 5B. Multicomponent membranes prone to phase separation could ensure a distinct composition and phase state of the ILV membrane (different from that of the GUV).[64] Furthermore, the microfluidic approach introduced here allows the subsequent loading of these compartments with solutions different from that in the vesicle interior/exterior, thus offering a pathway for performing localized and sub-compartmentalized processes such as protein synthesis or enzymatic reactions in a cell-like environment.

How easy it is to bend a flat membrane, for example when forming invaginations or outward buds, depends on the bending rigidity. The bending energy required to form a spherical bud from a flat membrane (of negligible spontaneous curvature) is $8\pi\kappa$. In the absence of an external pulling force, the direction of budding is defined by the membrane spontaneous curvature.[84] In the presence of EhVps20t, the vesicle membrane becomes stiffer (Figure 5C) but it does not exhibit buds and the spontaneous curvature remains close to zero. The latter curvature should then be induced by EhVps32. A number of mechanisms exist for generating and regulating the spontaneous curvature of membranes.[84,87,99] Both the bending rigidity (in heterogeneous membranes) and the spontaneous curvature can control the membrane shape (even to the extent of triggering membrane scission in membranes with fluid domains[90,100]). But these two membrane properties are often interrelated: the spontaneous curvature induced by adsorption or depletion layers, for instance, is inversely proportional to the bending rigidity[84] and thus, stiffer membranes would result in larger ILVs (i.e. would exhibit a spontaneous curvature which is lower in absolute magnitude). Entropic and steric effects between externally adsorbed proteins are typically expected to increase the magnitude of the spontaneous curvature of positive sign (i.e. the membrane tends to bulge more strongly toward the compartment containing the protein) with increasing coverage. Thus, adsorption of EhVps20t should intuitively lead to decreasing the magnitude of negative spontaneous curvature, which is consistent with the increase in ILV size (Figure 5). Thus, EhVps20t decreases the curvature magnitude (i) by entropic interactions and/or (ii) by effectively increasing the membrane bending rigidity.

Our results indicate that the size of the intraluminal buds is controlled not only by the EhVps20 concentration but also by the amount of EhVps32 present in the bulk whereby the two proteins influence the ILV size

antagonistically (Figure 5). To be able to resolve the process of ILV formation, we slowed down the reaction by reducing the concentration of EhVps32 (to 300 nM). This approach allowed us to observe the formation of EhVps32-rich domains and the subsequent formation of membrane buds in the region of these domains (Figure 4A), which has not been reported previously. Scission mediated by EhVps24 could result from reorganization of EhVps24 into assemblies that narrow the neck of the bud, as demonstrated for Vps24-induced Vps32 (Snf7) helical assemblies in.[28] Although ATPase activity by Vps4 may be essential for regulating the dynamic behavior of Vps32 filaments, here, we observe that EhVps32 has an intrinsic ability to self-associate forming homopolymers[101] (without the requirement of additional factors such as Vps4) as observed for the Vps32 homologue in *Caenorhabditis elegans*.[102] The minimal system of three ESCRT proteins as used here generates intraluminal vesicles in the absence of ATP, which provides a new and simpler pathway to vesicle division without the need to be concerned about any chemical energy supply. As recently demonstrated,[48] ESCRT-mediated budding in human cells is also a passive process driven by crowding of upstream ESCRTs (–0, -I and –II) coupled to a steep decrease in Gaussian curvature. The accumulation of upstream ESCRTs leads to recruitment of ESCRT-III/Vps4, which in turn triggers neck constriction and scission. Furthermore, in cells depleted of ESCRT-III, even though the overall ILV generation was impaired, their formation was still observed albeit at a lower degree, promoting the hypothesis that upstream ESCRTs initiate the membrane budding process through protein crowding[48] (similarly to previously reported effect of curvature modulation by GFP binding to membranes[103]) even though, after forming a bud neck, scission can be achieved also at low protein coverage.[90]

It would be interesting to investigate the structure of the EhVps32-rich domains with high-resolution techniques. These micron-sized domains appear to be transient and disassemble after the buds were fully formed (Figure 4A, bottom row), suggesting lateral mobility of the proteins bound to the vesicle surface. However, no diffusion of the membrane-bound proteins between the mother membrane and the buds could be detected in the FRAP measurements on bleached intraluminal buds (Figure 4B). In contrast, the underlying lipids partially recovered (Figure 4B). We speculate that the protein assembly around the membrane neck between the bud and the mother membrane as well as the anchor points of the protein assembly in the bud act as obstacles slowing down and obstructing lipid diffusion.

As shown in Figure 3, the buds open during osmotic inflation, whereas they do so only in a small fraction of vesicles when membrane tension is applied by micropipettes. The osmotic pressure acts to inflate and stretch the outer vesicle membrane and, as water permeates first through the vesicle membrane and then through the bud membrane to balance the osmotic differences. As a result, the bud gets inflated and its membrane expands/stretches as well ultimately leading to neck opening (note that the bud neck is relatively small to allow fast influx of solution to balance the osmolarity difference and the latter is mainly balanced through transmembrane permeation). Thus, the stress applied on the bud neck via osmotic inflation is imposed both from the increasing tension of the mother-vesicle as well as that of the bud membrane both pulling on the neck, see Figure 3E. The osmotic swelling of a 20 μm vesicle is established already in less than a second if we consider membrane permeability of about 15 μm/s,[104] and thus the tension in the membrane of intraluminal buds builds up almost immediately. In the case of aspirated vesicles, on the other hand, the tension is directly applied only to the mother-vesicle membrane whereas stress propagation to the bud might be impeded by the protein assembly in the bud neck region, see Figure 3F, which is consistent with the lack of recovery in the FRAP measurements. Further increase in the mother-vesicle tension then typically leads to vesicle rupture before the bud can open. This explains the difference in the observations that under osmotic inflation buds open, whereas they are unlikely to do so with a rapid increase of the suction pressure in the pipette. These findings indicate that experiments on bud stability as a function of membrane tension typically performed via osmotic swelling in the bulk (which is also easier than micropipette aspiration) might point to misleading conclusions regarding the effect of tension. Osmotic swelling experiments are also presumably less relevant considering that cells are rarely exposed to a large osmotic shock.

Considering the obtained results, the process of ILV formation in membranes mimicking endosomal composition as explored here is summarized in the sketch proposed in Figure 6B: EhVps20t homogeneously binds to the membrane (as shown in Figures 1 and 2), whereas EhVps32 generates clusters appearing as protein-rich domains (a few microns in size) at the vesicle surface. Over time, at the location of the domain, a nascent vesicle (bud) is formed (Figure 4A), which detaches only in the presence of EhVps24. Increase in

the membrane tension over the vesicle and the bud (as done with osmotic inflation) opens the bud distorting the scaffold formed by EhVps32. Upon tension release, new buds may reform only if previously unbound protein is present in the bulk (Figure 3). For slightly stiffer bare membranes, the mechanism is similar, however leading to larger bud and ILV size as in Figure 5. Our results demonstrate the competing roles of bending rigidity, which at low values facilitates closing the bud neck, and membrane tension, which acts in the opposite direction, namely, to open the neck.

Conclusion

In conclusion, we propose that the mechanism of ESCRT-III mediated scission starts with the binding of EhVps20 proteins to the membrane which act as nucleation sites for EhVps32 recruitment. In addition, EhVps20 increases the membrane stiffness, which competes with an increment in the spontaneous curvature triggered by EhVps32 incorporation. The balance of both forces produces intraluminal buds of various sizes depending on the concentration of the two proteins. The buds are stabilized by EhVps32 scaffolds (with immobilized protein but partially mobile lipids), which can be distorted on increased membrane tension leading to bud opening.

We demonstrated that a minimal set of only three ESCRT-III proteins is sufficient for fission of membrane necks. This finding is crucial for minimalistic approaches in synthetic biology aiming at reconstitution of cell division (with a minimal divisome).[90,92] We also showed that the size of ILVs is governed by the protein concentration and membrane bending rigidity. These two factors offer a route for controlling the size of intracellular organelles in artificial cells. The number of organelles (ILV) would depend on the area-to-volume ratio of the initial cell (GUV). Although microfluidic techniques for the production of nested vesicles in vesicles (vesosomes) allow direct mechanical control over the size of the different compartments (e.g.. via adjusting flow pressure and chip geometry), membranes created from double emulsions and/or oil/water phase transfer are not suitable for the reconstitution of proteins such as ATPases and other membrane enzymes because of the inherent leaflet-by-leaflet assembly of the membrane and the presence of oil. In contrast, the strategy of controlling compartment size via the interplay of ESCRT proteins and composition (modulating the membrane bending rigidity) is closer to nature and might offer new routes toward generation of smart synthetic cells. With the microfluidic technology used here, one is also able to load the different compartments with different solutions in a stepwise manner thus allowing for localized and compartmentalized processes as in cells. Presumably, establishing liquid ordered – liquid disordered phase separation in the membrane will allow to control also the compartment membrane composition with ILVs budding preferably from one type of membrane domain.[64,100] In the field of synthetic biology, microcompartmentalized vesicles are key to reverse-engineering of eukaryotic cells with reconstituted functionality.

Limitations of the study

As limitations of our studies, we cannot exclude that vesicles generated by electroformation exhibit some heterogeneity in terms of membrane composition, asymmetry and mechanics requiring larger statistics of measured data. In addition, before an ESCRT-generated bud is released from the mother vesicle, it must be connected to this vesicle via a closed membrane neck. In general, such a closed neck can be stabilized by spontaneous curvature, scaffold adhesion, or line tension of an intramembrane domain boundary.[70,76] So far, we have not been able to draw reliable conclusions about the relative importance of these different stabilization mechanisms, which remains an important challenge for future studies. Furthermore, we had not investigated the structure of the EhVps32-rich micron-sized domains, which appear to be transient and disassemble after the buds were fully formed (Figure 4A, bottom row). The application of high-resolution techniques in the future could shed some light in this direction.

STAR★METHODS

Detailed methods are provided in the online version of this paper and include the following:

- KEY RESOURCES TABLE
- RESOURCE AVAILABILITY
  - Lead contact
  - Materials availability
  - Data and code availability

SUPPLEMENTAL INFORMATION

Supplemental information can be found online at https://doi.org/10.1016/j.isci.2022.105765.

ACKNOWLEDGMENTS

We thank R. Seckler and S. Barbirz for kindly providing their facilities for protein purification and T. Seemann for microfabrication. We acknowledge input from R. B. Lira on the FRAP data. This work is part of the MaxSynBio consortium, which is jointly funded by the Federal Ministry of Education and Research of Germany and the Max Planck Society. Y. A-P. acknowledges the financial support by the European Commission under Horizon 2020's Marie Skłodowska-Curie Actions COFUND scheme (712754) and by the Severo Ochoa program of the Spanish Ministry of Science and Competitiveness [SEV-2014-0425 (2015–2019)].

AUTHOR CONTRIBUTIONS

Conceptualization, Y.A-P., E.O., R.L.. and R.D.; Investigation: Y.A-P., V.N.G., and E.E.; Methodology: Y.A-P., V.N.G., T.R.. and R.D.; Writing – Original Draft, Y.A-P., V.N.G., and R.D.; Writing – Review and Editing, Y.A-P., V.N.G., E.E., T.R., R.L., and R.D.; Resources, R.L. and R.D.; Supervision, R.D.

DECLARATION OF INTERESTS

The authors declare no competing interests.

INCLUSION AND DIVERSITY

We support inclusive, diverse, and equitable conduct of research.

Received: June 29, 2022
Revised: October 21, 2022
Accepted: December 6, 2022
Published: January 20, 2023

REFERENCES

1. Babst, M., Katzmann, D.J., Snyder, W.B., Wendland, B., and Emr, S.D. (2002). Endosome-associated complex, ESCRT-II, recruits transport machinery for protein sorting at the multivesicular body. Dev. Cell *3*, 283–289.

2. Babst, M., Katzmann, D.J., Estepa-Sabal, E.J., Meerloo, T., and Emr, S.D. (2002). Escrt-III: an endosome-associated heterooligomeric protein complex required for mvb sorting. Dev. Cell *3*, 271–282. https://doi.org/10.1016/s1534-5807(02)00220-4.

3. Katzmann, D.J., Babst, M., and Emr, S.D. (2001). Ubiquitin-dependent sorting into the multivesicular body pathway requires the function of a conserved endosomal protein sorting complex. Cell *106*, 145–155.

4. Katzmann, D.J., Odorizzi, G., and Emr, S.D. (2002). Receptor downregulation and multivesicular-body sorting. Nat. Rev. Mol. Cell Biol. *3*, 893–905. https://doi.org/10.1038/nrm973.

5. Morita, E., Sandrin, V., Alam, S.L., Eckert, D.M., Gygi, S.P., and Sundquist, W.I. (2007). Identification of human MVB12 proteins as ESCRT-I subunits that function in HIV budding. Cell Host Microbe *2*, 41–53.

6. Loncle, N., Agromayor, M., Martin-Serrano, J., and Williams, D.W. (2015). An ESCRT module is required for neuron pruning. Sci. Rep. *5*, 8461. https://doi.org/10.1038/srep08461.

7. Jimenez, A.J., Maiuri, P., Lafaurie-Janvore, J., Divoux, S., Piel, M., and Perez, F. (2014). ESCRT machinery is required for plasma membrane repair. Science *343*, 1247136.

8. Nabhan, J.F., Hu, R., Oh, R.S., Cohen, S.N., and Lu, Q. (2012). Formation and release of arrestin domain-containing protein 1-mediated microvesicles (ARMMs) at plasma membrane by recruitment of TSG101 protein. Proc. Natl. Acad. Sci. USA *109*, 4146–4151. https://doi.org/10.1073/pnas.1200448109.

9. Lee, J.-A., Beigneux, A., Ahmad, S.T., Young, S.G., and Gao, F.-B. (2007). ESCRT-III dysfunction causes autophagosome accumulation and neurodegeneration. Curr. Biol. *17*, 1561–1567. https://doi.org/10.1016/j.cub.2007.07.029.

10. Sahu, R., Kaushik, S., Clement, C.C., Cannizzo, E.S., Scharf, B., Follenzi, A., Potolicchio, I., Nieves, E., Cuervo, A.M., and Santambrogio, L. (2011). Microautophagy of cytosolic proteins by late endosomes. Dev. Cell *20*, 131–139. https://doi.org/10.1016/j.devcel.2010.12.003.

11. Christ, L., Raiborg, C., Wenzel, E.M., Campsteijn, C., and Stenmark, H. (2017). Cellular functions and molecular mechanisms of the ESCRT membrane-scission machinery. Trends Biochem. Sci. *42*, 42–56. https://doi.org/10.1016/j.tibs.2016.08.016.

12. Hurley, J.H., and Hanson, P.I. (2010). Membrane budding and scission by the ESCRT machinery: it's all in the neck. Nat. Rev. Mol. Cell Biol. *11*, 556–566. https://doi.org/10.1038/nrm2937.

13. Hurley, J.H. (2015). ESCRTs are everywhere. EMBO J. *34*, 2398–2407.

14. Pfitzner, A.-K., Moser von Filseck, J., and Roux, A. (2021). Principles of membrane remodeling by dynamic ESCRT-III polymers. Trends Cell Biol. *31*, 856–868. https://doi.org/10.1016/j.tcb.2021.04.005.

15. Remec Pavlin, M., and Hurley, J.H. (2020). The ESCRTs – converging on mechanism. J. Cell Sci. *133*, jcs240333. https://doi.org/10.1242/jcs.240333.

16. Samson, R.Y., Obita, T., Freund, S.M., Williams, R.L., and Bell, S.D. (2008). A role for the ESCRT system in cell division in archaea. Science *322*, 1710–1713. https://doi.org/10.1126/science.1165322.

17. Muzioł, T., Pineda-Molina, E., Ravelli, R.B., Zamborlini, A., Usami, Y., Göttlinger, H., and Weissenhorn, W. (2006). Structural basis for budding by the ESCRT-III factor CHMP3. Dev. Cell *10*, 821–830. https://doi.org/10.1016/j.devcel.2006.03.013.

18. Tang, S., Henne, W.M., Borbat, P.P., Buchkovich, N.J., Freed, J.H., Mao, Y., Fromme, J.C., and Emr, S.D. (2015). Structural basis for activation, assembly and membrane binding of ESCRT-III Snf7 filaments. Elife *4*, e12548. https://doi.org/10.7554/eLife.12548.

19. Bajorek, M., Schubert, H.L., McCullough, J., Langelier, C., Eckert, D.M., Stubblefield, W.M.B., Uter, N.T., Myszka, D.G., Hill, C.P., and Sundquist, W.I. (2009). Structural basis for ESCRT-III protein autoinhibition. Nat. Struct. Mol. Biol. *16*, 754–762. https://doi.org/10.1038/nsmb.1621.

20. Shim, S., Kimpler, L.A., and Hanson, P.I. (2007). Structure/function analysis of four core ESCRT-III proteins reveals common regulatory role for extreme C-terminal domain. Traffic *8*, 1068–1079. https://doi.org/10.1111/j.1600-0854.2007.00584.x.

21. Lee, I.-H., Kai, H., Carlson, L.-A., Groves, J.T., and Hurley, J.H. (2015). Negative membrane curvature catalyzes nucleation of endosomal sorting complex required for transport (ESCRT)-III assembly. Proc. Natl. Acad. Sci. USA *112*, 15892–15897. https://doi.org/10.1073/pnas.1518765113.

22. Moser von Filseck, J., Barberi, L., Talledge, N., Johnson, I.E., Frost, A., Lenz, M., and Roux, A. (2020). Anisotropic ESCRT-III architecture governs helical membrane tube formation. Nat. Commun. *11*, 1516. https://doi.org/10.1038/s41467-020-15327-4.

23. Schöneberg, J., Lee, I.-H., Iwasa, J.H., and Hurley, J.H. (2017). Reverse-topology membrane scission by the ESCRT proteins. Nat. Rev. Mol. Cell Biol. *18*, 5–17. https://doi.org/10.1038/nrm.2016.121.

24. Banjade, S., Tang, S., Shah, Y.H., and Emr, S.D. (2019). Electrostatic lateral interactions drive ESCRT-III heteropolymer assembly. Elife *8*, e46207. https://doi.org/10.7554/eLife.46207.

25. Adell, M.A.Y., Migliano, S.M., Upadhyayula, S., Bykov, Y.S., Sprenger, S., Pakdel, M., Vogel, G.F., Jih, G., Skillern, W., Behrouzi, R., et al. (2017). Recruitment dynamics of ESCRT-III and Vps4 to endosomes and implications for reverse membrane budding. Elife *6*, e31652. https://doi.org/10.7554/eLife.31652.

26. Banjade, S., Shah, Y.H., Tang, S., and Emr, S.D. (2021). Design principles of the ESCRT-III Vps24-Vps2 module. Elife *10*, e67709. https://doi.org/10.7554/eLife.67709.

27. Chiaruttini, N., and Roux, A. (2017). Dynamic and elastic shape transitions in curved ESCRT-III filaments. Curr. Opin. Cell Biol. *47*, 126–135. https://doi.org/10.1016/j.ceb.2017.07.002.

28. Henne, W.M., Buchkovich, N.J., Zhao, Y., and Emr, S.D. (2012). The endosomal sorting complex ESCRT-II mediates the assembly and architecture of ESCRT-III helices. Cell *151*, 356–371.

29. Agudo-Canalejo, J., and Lipowsky, R. (2018). Domes and cones: adhesion-induced fission of membranes by ESCRT proteins. PLoS Comput. Biol. *14*, e1006422. https://doi.org/10.1371/journal.pcbi.1006422.

30. Dimova, R., and Marques, C. (2019). The Giant Vesicle Book (Taylor & Francis Group, LLC). https://doi.org/10.1201/9781315152516.

31. Walde, P., Cosentino, K., Engel, H., and Stano, P. (2010). Giant vesicles: preparations and applications. Chembiochem *11*, 848–865.

32. Dimova, R., Aranda, S., Bezlyepkina, N., Nikolov, V., Riske, K.A., and Lipowsky, R. (2006). A practical guide to giant vesicles. Probing the membrane nanoregime via optical microscopy. J. Phys. Condens. Matter *18*, S1151–S1176.

33. Dimova, R. (2019). Giant vesicles and their use in assays for assessing membrane phase state, curvature, mechanics, and electrical properties. Annu. Rev. Biophys. *48*, 93–119. https://doi.org/10.1146/annurev-biophys-052118-115342.

34. Fenz, S.F., and Sengupta, K. (2012). Giant vesicles as cell models. Integr. Biol. *4*, 982–995.

35. Bertin, A., de Franceschi, N., de la Mora, E., Maity, S., Alqabandi, M., Miguet, N., di Cicco, A., Roos, W.H., Mangenot, S., Weissenhorn, W., and Bassereau, P. (2020). Human ESCRT-III polymers assemble on positively curved membranes and induce helical membrane tube formation. Nat. Commun. *11*, 2663. https://doi.org/10.1038/s41467-020-16368-5.

36. Ganzinger, K.A., and Schwille, P. (2019). More from less – bottom-up reconstitution of cell biology. J. Cell Sci. *132*, jcs227488. https://doi.org/10.1242/jcs.227488.

37. Schwille, P., Spatz, J., Landfester, K., Bodenschatz, E., Herminghaus, S., Sourjik, V., Erb, T.J., Bastiaens, P., Lipowsky, R., Hyman, A., et al. (2018). MaxSynBio: avenues towards creating cells from the bottom up. Angew. Chem. Int. Ed. Engl. *57*, 13382–13392. https://doi.org/10.1002/anie.201802288.

38. Göpfrich, K., Platzman, I., and Spatz, J.P. (2018). Mastering complexity: towards bottom-up construction of Multifunctional eukaryotic synthetic cells. Trends Biotechnol. *36*, 938–951. https://doi.org/10.1016/j.tibtech.2018.03.008.

39. Rideau, E., Dimova, R., Schwille, P., Wurm, F.R., and Landfester, K. (2018). Liposomes and polymersomes: a comparative review towards cell mimicking. Chem. Soc. Rev. *47*, 8572–8610. https://doi.org/10.1039/C8CS00162F.

40. Weiss, M., Frohnmayer, J.P., Benk, L.T., Haller, B., Janiesch, J.-W., Heitkamp, T., Börsch, M., Lira, R.B., Dimova, R., Lipowsky, R., et al. (2018). Sequential bottom-up assembly of mechanically stabilized synthetic cells by microfluidics. Nat. Mater. *17*, 89–96. https://doi.org/10.1038/nmat5005.

41. Avalos-Padilla, Y., Knorr, R.L., Javier-Reyna, R., García-Rivera, G., Lipowsky, R., Dimova, R., and Orozco, E. (2018). The conserved ESCRT-III machinery participates in the phagocytosis of Entamoeba histolytica.

Front. Cell. Infect. Microbiol. *8*, 53. https://doi.org/10.3389/fcimb.2018.00053.

42. Im, Y.J., Wollert, T., Boura, E., and Hurley, J.H. (2009). Structure and function of the ESCRT-II-III interface in multivesicular body biogenesis. Dev. Cell *17*, 234–243. https://doi.org/10.1016/j.devcel.2009.07.008.

43. Wollert, T., Wunder, C., Lippincott-Schwartz, J., and Hurley, J.H. (2009). Membrane scission by the ESCRT-III complex. Nature *458*, 172–177. https://doi.org/10.1038/nature07836.

44. Booth, A., Marklew, C.J., Ciani, B., and Beales, P.A. (2019). In vitro membrane remodeling by ESCRT is regulated by negative feedback from membrane tension. iScience *15*, 173–184. https://doi.org/10.1016/j.isci.2019.04.021.

45. De Franceschi, N., Alqabandi, M., Miguet, N., Caillat, C., Mangenot, S., Weissenhorn, W., and Bassereau, P. (2018). The ESCRT protein CHMP2B acts as a diffusion barrier on reconstituted membrane necks. J. Cell Sci. *132*, jcs217968. https://doi.org/10.1242/jcs.217968.

46. Schöneberg, J., Pavlin, M.R., Yan, S., Righini, M., Lee, I.-H., Carlson, L.-A., Bahrami, A.H., Goldman, D.H., Ren, X., Hummer, G., et al. (2018). ATP-dependent force generation and membrane scission by ESCRT-III and Vps4. Science *362*, 1423–1428. https://doi.org/10.1126/science.aat1839.

47. Nguyen, H.C., Talledge, N., McCullough, J., Sharma, A., Moss, F.R., Iwasa, J.H., Vershinin, M.D., Sundquist, W.I., and Frost, A. (2020). Membrane constriction and thinning by sequential ESCRT-III polymerization. Nat. Struct. Mol. Biol. *27*, 392–399. https://doi.org/10.1038/s41594-020-0404-x.

48. Liese, S., Wenzel, E.M., Kjos, I., Rojas Molina, R., Schultz, S.W., Brech, A., Stenmark, H., Raiborg, C., and Carlson, A. (2020). Protein crowding mediates membrane remodeling in upstream ESCRT-induced formation of intraluminal vesicles. Proc. Natl. Acad. Sci. USA *117*, 28614–28624. https://doi.org/10.1073/pnas.2014228117.

49. Alqabandi, M., de Franceschi, N., Maity, S., Miguet, N., Bally, M., Roos, W.H., Weissenhorn, W., Bassereau, P., and Mangenot, S. (2021). The ESCRT-III isoforms CHMP2A and CHMP2B display different effects on membranes upon polymerization. BMC Biol. *19*, 66. https://doi.org/10.1186/s12915-021-00983-9.

50. Booth, A., Marklew, C.J., Ciani, B., and Beales, P.A. (2021). The influence of phosphatidylserine localisation and lipid phase on membrane remodelling by the ESCRT-II/ESCRT-III complex. Faraday Discuss *232*, 188–202. https://doi.org/10.1039/D0FD00042F.

51. Deng, N.-N., Yelleswarapu, M., Zheng, L., and Huck, W.T.S. (2017). Microfluidic assembly of monodisperse vesosomes as artificial cell models. J. Am. Chem. Soc. *139*, 587–590. https://doi.org/10.1021/jacs.6b10977.

52. Deshpande, S., Spoelstra, W.K., van Doorn, M., Kerssemakers, J., and Dekker, C. (2018). Mechanical division of cell-sized liposomes. ACS Nano *12*, 2560–2568. https://doi.org/10.1021/acsnano.7b08411.

53. Göpfrich, K., Haller, B., Staufer, O., Dreher, Y., Mersdorf, U., Platzman, I., and Spatz, J.P. (2019). One-pot assembly of complex giant unilamellar vesicle-based synthetic cells. ACS Synth. Biol. *8*, 937–947. https://doi.org/10.1021/acssynbio.9b00034.

54. Li, S., Wang, X., Mu, W., and Han, X. (2019). Chemical signal communication between two protoorganelles in a lipid-based artificial cell. Anal. Chem. *91*, 6859–6864. https://doi.org/10.1021/acs.analchem.9b01128.

55. Karimi, M., Steinkühler, J., Roy, D., Dasgupta, R., Lipowsky, R., and Dimova, R. (2018). Asymmetric ionic conditions generate large membrane curvatures. Nano Lett. *18*, 7816–7821. https://doi.org/10.1021/acs.nanolett.8b03584.

56. Bezlyepkina, N., Gracià, R.S., Shchelokovskyy, P., Lipowsky, R., and Dimova, R. (2013). Phase diagram and tie-line determination for the ternary mixture DOPC/eSM/Cholesterol. Biophys. J. *104*, 1456–1464.

57. Steinkühler, J., De Tillieux, P., Knorr, R.L., Lipowsky, R., and Dimova, R. (2018). Charged giant unilamellar vesicles prepared by electroformation exhibit nanotubes and transbilayer lipid asymmetry. Sci. Rep. *8*, 11838. https://doi.org/10.1038/s41598-018-30286-z.

58. Yandrapalli, N., and Robinson, T. (2019). Ultra-high capacity microfluidic trapping of giant vesicles for high-throughput membrane studies. Lab Chip *19*, 626–633. https://doi.org/10.1039/C8LC01275J.

59. Guha, S., Rajani, M., and Padh, H. (2007). Identification and characterization of lipids from endosomes purified by electromagnetic chromatography. Indian J. Biochem. Biophys. *44*, 443–449.

60. Sztolsztener, M.E., Dobrzyn, A., Pikula, S., Tylki-Szymanska, A., and Bandorowicz-Pikula, J. (2012). Impaired dynamics of the late endosome/lysosome compartment in human Niemann-Pick type C skin fibroblasts carrying mutation in NPC1 gene. Mol. Biosyst. *8*, 1197–1205. https://doi.org/10.1039/c2mb05447g.

61. Kubsch, B., Robinson, T., Steinkühler, J., and Dimova, R. (2017). Phase behavior of charged vesicles under symmetric and asymmetric solution conditions monitored with fluorescence microscopy. J. Vis. Exp. *128*, e56034. https://doi.org/10.3791/56034.

62. Saksena, S., Wahlman, J., Teis, D., Johnson, A.E., and Emr, S.D. (2009). Functional reconstitution of ESCRT-III assembly and disassembly. Cell *136*, 97–109. https://doi.org/10.1016/j.cell.2008.11.013.

63. Chiaruttini, N., Redondo-Morata, L., Colom, A., Humbert, F., Lenz, M., Scheuring, S., and Roux, A. (2015). Relaxation of loaded ESCRT-III spiral springs drives membrane deformation. Cell *163*, 866–879. https://doi.org/10.1016/j.cell.2015.10.017.

64. Avalos-Padilla, Y., Georgiev, V.N., and Dimova, R. (2021). ESCRT-III induces phase separation in model membranes prior to budding and causes invagination of the liquid-ordered phase. Biochim. Biophys. Acta. Biomembr. *1863*, 183689. https://doi.org/10.1016/j.bbamem.2021.183689.

65. Weinberger, A., Walter, V., MacEwan, S.R., Schmatko, T., Muller, P., Schroder, A.P., Chilkoti, A., and Marques, C.M. (2017). Cargo self-assembly rescues affinity of cell-penetrating peptides to lipid membranes. Sci. Rep. *7*, 43963. https://doi.org/10.1038/srep43963. https://www.nature.com/articles/srep43963#supplementary-information.

66. Kucerka, N., Tristram-Nagle, S., and Nagle, J.F. (2005). Structure of fully hydrated fluid phase lipid bilayers with monounsaturated chains. J. Membr. Biol. *208*, 193–202.

67. Mukhopadhyay, P., Monticelli, L., and Tieleman, D.P. (2004). Molecular dynamics simulation of a palmitoyl-oleoyl phosphatidylserine bilayer with Na+ counterions and NaCl. Biophys. J. *86*, 1601–1609. https://doi.org/10.1016/S0006-3495(04)74227-7.

68. Snead, W.T., Hayden, C.C., Gadok, A.K., Zhao, C., Lafer, E.M., Rangamani, P., and Stachowiak, J.C. (2017). Membrane fission by protein crowding. Proc. Natl. Acad. Sci. USA *114*, E3258–E3267.

69. Bhatia, T., Christ, S., Steinkühler, J., Dimova, R., and Lipowsky, R. (2020). Simple sugars shape giant vesicles into multispheres with many membrane necks. Soft Matter *16*, 1246–1258. https://doi.org/10.1039/C9SM01890E.

70. Lipowsky, R. (2019). Understanding giant vesicles: a theoretical perspective. In The Giant Vesicle Book, R. Dimova and C. Marques, eds. (Taylor & Francis Group, LLC), pp. 73–168. https://doi.org/10.1201/9781315152516.

71. Seifert, U., Berndl, K., and Lipowsky, R. (1991). Shape transformations of vesicles: phase diagram for spontaneous-curvature and bilayer-coupling models. Phys. Rev. A *44*, 1182–1202.

72. Frankel, E.B., Shankar, R., Moresco, J.J., Yates, J.R., Volkmann, N., and Audhya, A. (2017). Ist1 regulates ESCRT-III assembly and function during multivesicular endosome biogenesis in Caenorhabditis elegans embryos. Nat. Commun. *8*, 1439. https://doi.org/10.1038/s41467-017-01636-8.

73. Buono, R.A., Leier, A., Paez-Valencia, J., Pennington, J., Goodman, K., Miller, N., Ahlquist, P., Marquez-Lago, T.T., and Otegui, M.S. (2017). ESCRT-mediated vesicle concatenation in plant endosomes. J. Cell Biol. *216*, 2167–2177. https://doi.org/10.1083/jcb.201612040.

74. Babst, M., Wendland, B., Estepa, E.J., and Emr, S.D. (1998). The Vps4p AAA ATPase regulates membrane association of a Vps protein complex required for normal endosome function. EMBO J. *17*, 2982–2993. https://doi.org/10.1093/emboj/17.11.2982.

75. Lata, S., Schoehn, G., Jain, A., Pires, R., Piehler, J., Gottlinger, H.G., and Weissenhorn, W. (2008). Helical structures of ESCRT-III are disassembled by VPS4. Science *321*, 1354–1357. https://doi.org/10.1126/science.1161070.

76. Agudo-Canalejo, J., and Lipowsky, R. (2015). Critical particle sizes for the engulfment of nanoparticles by membranes and vesicles with bilayer asymmetry. ACS Nano *9*, 3704–3720. https://doi.org/10.1021/acsnano.5b01285.

77. Faizi, H.A., Reeves, C.J., Georgiev, V.N., Vlahovska, P.M., and Dimova, R. (2020). Fluctuation spectroscopy of giant unilamellar vesicles using confocal and phase contrast microscopy. Soft Matter *16*, 8996–9001. https://doi.org/10.1039/D0SM00943A.

78. Gracià, R.S., Bezlyepkina, N., Knorr, R.L., Lipowsky, R., and Dimova, R. (2010). Effect of cholesterol on the rigidity of saturated and unsaturated membranes: fluctuation and electrodeformation analysis of giant vesicles. Soft Matter *6*, 1472–1482. https://doi.org/10.1039/b920629a.

79. Faizi, H.A., Frey, S.L., Steinkühler, J., Dimova, R., and Vlahovska, P.M. (2019). Bending rigidity of charged lipid bilayer membranes. Soft Matter *15*, 6006–6013. https://doi.org/10.1039/C9SM00772E.

80. Henriksen, J., Rowat, A.C., Brief, E., Hsueh, Y.W., Thewalt, J.L., Zuckermann, M.J., and Ipsen, J.H. (2006). Universal behavior of membranes with sterols. Biophys. J. *90*, 1639–1649.

81. Pan, J., Mills, T.T., Tristram-Nagle, S., and Nagle, J.F. (2008). Cholesterol perturbs lipid bilayers nonuniversally. Phys. Rev. Lett. *100*, 198103.

82. Nagle, J.F., Evans, E.A., Bassereau, P., Baumgart, T., Tristram-Nagle, S., and Dimova, R. (2021). A needless but interesting controversy. Proc. Natl. Acad. Sci. USA *118*. e2025011118. https://doi.org/10.1073/pnas.2025011118.

83. Dimova, R. (2014). Recent developments in the field of bending rigidity measurements on membranes. Adv. Colloid Interface Sci. *208*, 225–234. https://doi.org/10.1016/j.cis.2014.03.003.

84. Lipowsky, R. (2013). Spontaneous tubulation of membranes and vesicles reveals membrane tension generated by spontaneous curvature. Faraday Discuss *161*, 305–331. discussion 419-459.

85. Liu, Y., Agudo-Canalejo, J., Grafmüller, A., Dimova, R., and Lipowsky, R. (2016). Patterns of flexible nanotubes formed by liquid-ordered and liquid-disordered membranes. ACS Nano *10*, 463–474. https://doi.org/10.1021/acsnano.5b05377.

86. Nikolov, V., Lipowsky, R., and Dimova, R. (2007). Behavior of giant vesicles with anchored DNA molecules. Biophys. J. *92*, 4356–4368.

87. Bassereau, P., Jin, R., Baumgart, T., Deserno, M., Dimova, R., Frolov, V.A., Bashkirov, P.V., Grubmüller, H., Jahn, R., Risselada, H.J., et al. (2018). The 2018 biomembrane curvature and remodeling roadmap. J. Phys. D Appl. Phys. *51*, 343001.

88. Frolov, V.A., Escalada, A., Akimov, S.A., and Shnyrova, A.V. (2015). Geometry of membrane fission. Chem. Phys. Lipids *185*, 129–140. https://doi.org/10.1016/j.chemphyslip.2014.07.006.

89. McMahon, H.T., and Boucrot, E. (2015). Membrane curvature at a glance. J. Cell Sci. *128*, 1065–1070. https://doi.org/10.1242/jcs.114454.

90. Steinkühler, J., Knorr, R.L., Zhao, Z., Bhatia, T., Bartelt, S.M., Wegner, S., Dimova, R., and Lipowsky, R. (2020). Controlled division of cell-sized vesicles by low densities of membrane-bound proteins. Nat. Commun. *11*, 905. https://doi.org/10.1038/s41467-020-14696-0.

91. Marklew, C.J., Booth, A., Beales, P.A., and Ciani, B. (2018). Membrane remodelling by a lipidated endosomal sorting complex required for transport-III chimera, in vitro. Interface Focus *8*, 20180035. https://doi.org/10.1098/rsfs.2018.0035.

92. Kretschmer, S., Ganzinger, K.A., Franquelim, H.G., and Schwille, P. (2019). Synthetic cell division via membrane-transforming molecular assemblies. BMC Biol. *17*, 43. https://doi.org/10.1186/s12915-019-0665-1.

93. Sorkin, A., and von Zastrow, M. (2009). Endocytosis and signalling: intertwining molecular networks. Nat. Rev. Mol. Cell Biol. *10*, 609–622. https://doi.org/10.1038/nrm2748.

94. Pfitzner, A.-K., Mercier, V., Jiang, X., Moser von Filseck, J., Baum, B., Šarić, A., and Roux, A. (2020). An ESCRT-III polymerization sequence drives membrane deformation and fission. Cell *182*, 1140–1155.e18. https://doi.org/10.1016/j.cell.2020.07.021.

95. Obita, T., Saksena, S., Ghazi-Tabatabai, S., Gill, D.J., Perisic, O., Emr, S.D., and Williams, R.L. (2007). Structural basis for selective recognition of ESCRT-III by the AAA ATPase Vps4. Nature *449*, 735–739. https://doi.org/10.1038/nature06171.

96. Fyfe, I., Schuh, A.L., Edwardson, J.M., and Audhya, A. (2011). Association of the endosomal sorting complex ESCRT-II with the Vps20 subunit of ESCRT-III generates a curvature-sensitive complex capable of nucleating ESCRT-III filaments. J. Biol. Chem. *286*, 34262–34270. https://doi.org/10.1074/jbc.M111.266411.

97. Teis, D., Saksena, S., Judson, B.L., and Emr, S.D. (2010). ESCRT-II coordinates the assembly of ESCRT-III filaments for cargo sorting and multivesicular body vesicle formation. EMBO J. *29*, 871–883. https://doi.org/10.1038/emboj.2009.408.

98. Cashikar, A.G., Shim, S., Roth, R., Maldazys, M.R., Heuser, J.E., and Hanson, P.I. (2014). Structure of cellular ESCRT-III spirals and their relationship to HIV budding. Elife *3*, e02184. https://doi.org/10.7554/eLife.02184.

99. Zimmerberg, J., and Kozlov, M.M. (2006). How proteins produce cellular membrane curvature. Nat. Rev. Mol. Cell Biol. *7*, 9–19. https://doi.org/10.1038/nrm1784.

100. Lipowsky, R. (1993). Domain-induced budding of fluid membranes. Biophys. J. *64*, 1133–1138. https://doi.org/10.1016/S0006-3495(93)81479-6.

101. Avalos-Padilla, Y., Betanzos, A., Javier-Reyna, R., García-Rivera, G., Chávez-Munguía, B., Lagunes-Guillén, A., Ortega, J., and Orozco, E. (2015). EhVps32 is a vacuole-associated protein involved in pinocytosis and phagocytosis of entamoeba histolytica. PLoS Pathog. *11*, e1005079. https://doi.org/10.1371/journal.ppat.1005079.

102. Shen, Q.-T., Schuh, A.L., Zheng, Y., Quinney, K., Wang, L., Hanna, M., Mitchell, J.C., Otegui, M.S., Ahlquist, P., Cui, Q., and Audhya, A. (2014). Structural analysis and modeling reveals new mechanisms governing ESCRT-III spiral filament assembly. J. Cell Biol. *206*, 763–777. https://doi.org/10.1083/jcb.201403108.

103. Stachowiak, J.C., Schmid, E.M., Ryan, C.J., Ann, H.S., Sasaki, D.Y., Sherman, M.B., Geissler, P.L., Fletcher, D.A., and Hayden, C.C. (2012). Membrane bending by protein-protein crowding. Nat. Cell Biol. *14*, 944–949. https://doi.org/10.1038/Ncb2561.

104. Bhatia, T., Robinson, T., and Dimova, R. (2020). Membrane permeability to water measured by microfluidic trapping of giant vesicles. Soft Matter *16*, 7359–7369. https://doi.org/10.1039/D0SM00155D.

105. Angelova, M.I., and Dimitrov, D.S. (1986). Liposome electroformation. Faraday Discuss. Chem. Soc. *81*, 303–311.

106. Henriksen, J.R., and Ipsen, J.H. (2002). Thermal undulations of quasi-spherical vesicles stabilized by gravity. Eur. Phys. J. E Soft Matter *9*, 365–374.

107. Vitkova, V., Mitkova, D., Antonova, K., Popkirov, G., and Dimova, R. (2018). Sucrose solutions alter the electric capacitance and dielectric permittivity of lipid bilayers. Colloids Surf. A Physicochem. Eng. Asp. *557*, 51–57. https://doi.org/10.1016/j.colsurfa.2018.05.011.

108. Hunter, R.J. (1981). In Zeta Potential in Colloid Science, R.J. Hunter, ed. (Academic Press). https://doi.org/10.1016/B978-0-12-361961-7.50007-9.

109. Klasczyk, B., Knecht, V., Lipowsky, R., and Dimova, R. (2010). Interactions of alkalimetal chlorides with phosphatidylcholine vesicles. Langmuir *26*, 18951–18958.

110. Holz, M., Heil, S.R., and Sacco, A. (2000). Temperature-dependent self-diffusion coefficients of water and six selected molecular liquids for calibration in accurate 1H NMR PFG measurements. Phys. Chem. Chem. Phys. *2*, 4740–4742. https://doi.org/10.1039/B005319H.

111. Lira, R.B., Steinkühler, J., Knorr, R.L., Dimova, R., and Riske, K.A. (2016). Posing for a picture: vesicle immobilization in agarose gel. Sci. Rep. *6*, 25254. https://doi.org/10.1038/srep25254.

112. Kang, M., Day, C.A., Kenworthy, A.K., and DiBenedetto, E. (2012). Simplified equation to extract diffusion coefficients from confocal FRAP data. Traffic *13*, 1589–1600. https://doi.org/10.1111/tra.12008.

113. Henriksen, J.R., and Ipsen, J.H. (2004). Measurement of membrane elasticity by micro-pipette aspiration. Eur. Phys. J. E. Soft Matter *14*, 149–167.

STAR★METHODS

KEY RESOURCES TABLE

REAGENT or RESOURCE	SOURCE	IDENTIFIER
Bacterial and virus strains		
Escherichia coli BL21(DE3)pLysS/p *GEX6P-Ehvps20*	Ref.[41]	N/A
Escherichia coli BL21(DE3)pLysS/p *GEX6P-Ehvps20 (1–173)*	Ref.[41]	N/A
Escherichia coli BL21(DE3)pLysS/p *GEX6P-Ehvps24*	Ref.[41]	N/A
Escherichia coli BL21(DE3)pLysS/p *GEX6P-Ehvps32*	Ref.[41]	N/A
Chemicals, peptides, and recombinant proteins		
Isopropyl β-D-thiogalactoside (IPTG)	Sigma-Aldrich	I6758; CAS: 367-93-1
Pre-Scission protease enzyme	GE-Healthcare	Cat#27-0843-01
Oregon Green™ 488 Carboxylic Acid, Succinimidyl Ester, 5-isomer	Thermo Fisher	Cat#O6147
1-palmitoyl-2/oleoyl-*sn*-glycero-3-phos phocholine (POPC)	Avanti Polar Lipids	Cat#850457
1-palmitoyl-2-oleoyl-*sn*-glycero-3-phos phoserine (POPS)	Avanti Polar Lipids	Cat#840034
Cholesterol (Chol)	Avanti Polar Lipids	Cat#700000
1,2-dioleoyl-*sn*-glycero-3-phospho-(1′-myo-inositol-3′-phosphate) (PI(3)P)	Avanti Polar Lipids	Cat#850150
Texas Red® 1,2-dihexadecanoyl- sn-*glycero*-3-phosphoethanolamine (TR-DHPE)	Invitrogen	Cat#T1365MP
1,1′-dioctadecyl-3,3,3′,3′-tetramethylindocar bocyanine perchlorate ($DiIC_{18}$)	Invitrogen	Cat#D307
Poly(dimethylsiloxane) (PDMS)	Sigma-Aldrich	93,388; CAS: 63,148-62-9
BSA	Sigma-Aldrich	Cat#A8806
Software and algorithms		
OriginPro	OriginLab Corp.	https://www.originlab.com/index.aspx?go=PRODUCTS/Origin
ImageJ	Schneider et al., 2012	https://imagej.nih.gov/ij/
Radial Profile Extended Plugin	Philippe Carl	http://questpharma.u-strasbg.fr/html/radial-profile-ext.html
Other		
Superdex 200 16/600 column	GE-Healthcare	Cat#28-9893-35
Äkta-Purifier FPLC	GE-Healthcare	https://www.cytivalifesciences.com/en/us/shop/chromatography/chromatography-systems/akta-go-protein-purification-system-p-11219
Osmomat 030	Gonotec	Osmomat 3000 freezing point osmometer
TCS SP8 confocal microscope	Leica	https://www.leica-microsystems.com/products/confocal-microscopes/p/leica-tcs-sp5/
Silanised 4″ silicon wafers with master forms at a height of 40 μm	Yandrapalli and Robinson, 2018 (DOI: 10.1039/C8LC01275J)	N/A

(*Continued on next page*)

Continued

REAGENT or RESOURCE	SOURCE	IDENTIFIER
1.5 mm biopsy puncher	Kai Europe GmbH	https://www.kai-europe.com/medical/biopsiestanzen_auswurf.php?lang=en
Plasma Cleaner	Harrick Plasma	Cat#PDC-002-CE
neMESYS syringe pump	Cetoni	https://cetoni.com/?gclid=EAIaIQobChMIn_PvqfHD-AIVxo9oCR3P8QRzEAAYASAAEgKstfD_BwE
Axio Observer D1 microscope	Zeiss	https://www.zeiss.com/microscopy/int/products/light-microscopes/axio-observer-for-biology.html
digital camera (pco.edge)	PCO AG	https://www.pco.de/
Polycarbonate membranes 100 nm (Whatman® Nuclepore™ Track-Etched Membranes)	Sigma	WHA110605 https://www.sigmaaldrich.com/DE/en/product/aldrich/wha110605
LiposoFast pneumatic extruder	Avestin	http://www.avestin.com/liposome%20extruders.htm
Zetasizer Nano ZS	Malvern Instruments	https://www.malvernpanalytical.com/en/support/product-support/zetasizer-range/zetasizer-nano-range?campaignid=31870140&adgroupid=62424583093&creative=314787143223&keyword=&matchtype=&network=g&device=c&gclid=EAIaIQobChMIoZyIlvPD-AIVXI9oCR3x0AY3EAAYASAAEgJTPPD_BwE
Folded capillary cells with integral gold electrodes	Malvern	Cat#DST1060
Borosilicate capillaries	World Precision Instruments Inc.	Cat#1B100-4
Pipette puller	Sutter Instruments	Model P-97
Linear translational stage	Physik Instrumente	Cat#IM-531.PD

RESOURCE AVAILABILITY

Lead contact

Information and requests for resources should be directed to and will be fulfilled by the corresponding author, Rumiana Dimova (Rumiana.Dimova@mpikg.mpg.de).

Materials availability

This study did not generate new unique materials or reagents.

Data and code availability

Any additional information (including Microscopy data) required to reanalyze the data reported in this paper is available from the lead contact upon reasonable request.

EXPERIMENTAL MODEL AND SUBJECT DETAILS

Expression and purification of recombinant proteins

Escherichia coli BL21(DE3)pLysS cells transformed with the different plasmids used in this study were cultured in Terrific broth medium (T5574, Sigma-Aldrich) supplemented with 100 μg/mL Ampicillin (A9518, Sigma-Aldrich). To achieve exponential growth (OD_{600} ~ 0.6), cells were grown at 37 °C and 180 rpm, whereas to induce protein expression, temperature was lowered to 16 °C.

METHOD DETAILS

Expression and purification of recombinant proteins

Recombinant proteins were purified as previously.[41] Briefly, proteins were induced overnight by addition of 0.5 mM of IPTG (I6758, Sigma-Aldrich) to produce GST-rEhVps20, GST-rEhVps20t, GST-rEhVps24 and GST-rEhVps32 tagged proteins. Purified GST-tagged proteins were dialyzed against the buffer for the Pre-Scission protease enzyme (27-0843-01, GE-healthcare) and the GST-tags were removed according to manufacturer's instructions. GST-free monomers were subsequently purified by size exclusion

chromatography with a Superdex 200 16/600 column (28-9893-35, GE-healthcare) connected to an Äkta-Purifier FPLC (GE-healthcare). Proteins were stored at −80 °C in 50 mM Tris, 300 mM NaCl, pH = 7.4 buffer at concentrations between 60 and 10 μM.

Labeling of recombinant proteins

The recombinant proteins EhVps20, EhVps20t and EhVps32 were labeled using Oregon Green 488 (OG) (O6147, Thermo Fisher) following the manufacturer's protocol. The labeled and unlabelled proteins were separated by size exclusion chromatography with a Superdex 200 16/600 column (GE28-9893-35, GE-healthcare) connected to an Äkta-Purifier FPLC (GE-healthcare). The degree of labeling was assessed according to manufacturer's instructions. In all cases, we used 1:4 ratio of labeled: unlabelled proteins to maintain activity.

Preparation and imaging of giant unilamellar vesicles

The lipids 1-palmitoyl-2-oleoyl-*sn*-glycero-3-phosphocholine (POPC, 850,457) 1-palmitoyl-2-oleoyl-*sn*-glycero-3-phosphoserine (POPS, 840,034), cholesterol (Chol, 700,000) and 1,2-dioleoyl-*sn*-glycero-3-phospho-(1′-myo-inositol-3′-phosphate) (PI(3)P, 850,150) were purchased from Avanti Polar Lipids, Alabaster IL. In all cases, we added either Texas Red 1,2-dihexadecanoyl-*sn*-glycero-3-phosphoethanolamine (TR-DHPE) (T1365MP, Invitrogen) or $DiIC_{18}$ (1,1′-dioctadecyl-3,3,3′,3′-tetramethylindocarbocyanine perchlorate, D307, Invitrogen) at a concentration of 0.1 mol % in the lipid mixtures for the visualization of the membranes. Giant unilamellar vesicles of different lipid compositions were grown using the electroformation method.[105] Briefly, 10 μL of a 4 mM lipid stock solution in chloroform were spread on indium tin oxide (ITO) coated glasses. The excess of chloroform was eliminated under vacuum at room temperature (RT) for 1h. Then, ITO-glasses were assembled with a 2 mm-thick Teflon spacer between them to form the electroformation chamber, which, if not indicated otherwise, was filled with a 600 mM sucrose solution that matched the osmolarity of the buffer containing the proteins (~650 mOsm/Kg). Osmolarities were controlled and adjusted using an osmometer (Osmomat 030, Gonotec, Germany). Finally, an electric AC-field (1.6 V, 10 Hz) was applied for 1 h at different temperatures (60 °C for GUVs that contain PI(3)P and RT for the rest of the compositions). GUVs were collected and cooled to RT before use. Confocal imaging was performed on a Leica TCS SP8 confocal microscope (Mannheim, Germany). $DiIC_{18}$ was excited with a diode-pumped solid-state laser 561 nm laser, OG with a 488 nM line of Argon laser and TR-DHPE was excited with the Helium-Neon-laser at 594 nm. To avoid crosstalk between the different fluorescence signals, a sequential scanning was performed. For the $DiIC_{18}$ dye, the fluorescence signal was collected in the ranges of 580–700 nm. The fluorescence signal of OG was collected between 495 and 530 nm and the fluorescence signal of TR-DHPE was collected between 610 and 750 nm. The gain and laser intensity was maintained fixed for all experiments.

Microfluidic chamber

We used a microfluidic device to follow the effect of ESCRT proteins on the same GUV and to observe the action of each individual added protein. The design and fabrication of the device has been detailed elsewhere.[58] The PDMS chips were produced using standard soft photolithography as follows. Master forms at a height of 40 μm were produced on a 4″ silicon wafer (Si-Mat) by UV exposure of SU8-3025 (Microchem). Before use, they were salinized in an overnight atmosphere of 1,1,2H,2H-perfluorodecyltrichlorosilane (729,965, Sigma-Aldrich) to prevent unwanted adhesion of PDMS. PDMS was mixed with the curing agent in 10:1 ratio, degassed for 30 min, and subsequently poured on top of the master form to a height of approximately 5 mm. After a further degassing for 30 min, the PDMS covered wafer was heat cured at 90 °C for 3 h. Afterward, the PDMS was separated from the wafer and chips were cut out. Fluidic access holes were punched with a 1.5 mm biopsy puncher (Kai Europe GmbH). A sample reservoir, made from a cut pipette tip was sealed on top of the inlet with PDMS and cured at 90 °C for 30 min. Finally, the device was assembled by bonding the PDMS chip to a glass coverslip by an air plasma treatment (Plasma Cleaner PDC-002-CE, Harrick Plasma) at 0.6 mbar for 1 min. Bonding was aided by an additional 60 °C for 2 h before use.

For the sequential protein binding experiments, microfluidic devices were coated with 2% BSA, A8806, Sigma Aldrich) dissolved in the protein buffer (25 mM Tris, 150 mM NaCl, pH = 7.4). Then, 100 μL of GUVs, pre-deflated using a buffer of 5% higher osmolarity (adjusted with glucose), were loaded into the microfluidic device at a flow rate of 10 μL/min using a syringe pump (neMESYS, cetoni) to control the flow (Figure S1). The GUV buffer was exchanged with 100 μL of the isotonic protein buffer (25 mM Tris,

150 mM NaCl, pH 7.4) at a flow of 5 μL/min. Afterward, the protein EhVps20t was added to the chamber to yield a final concentration of 125 nM, with a flow of 0.1 μL/min, then EhVps32 (600 nM) and EhVps24 (200 nM) were added in that order while maintaining the flow rate in the whole experiment. Similarly, GUVs were incubated with six rounds of buffer as a negative control (Figure S2).

To monitor the protein-domain formation shown in Figure 4, POPC:POPS:Chol:PI(3)P (62:10:25:3) GUVs were loaded in a microfluidic device following the protocol described above. Then, Ehvps20t and EhVps32 were added to the chamber simultaneously to achieve a final concentration of 125 nM and 300 nM respectively, at a flow of 0.1 μL/min. Finally, EhVps24 (200 nM) was flushed in at the same flow rate. In this case, at least 30 GUVs present in the microfluidic traps were followed throughout the whole experiment.

Fluctuation analysis

Fluctuation analysis was performed according to the protocol described earlier.[78] GUVs composed of POPC:POPS:Chol:PI(3)P (62:10:25:3) and (52:10:35:3) were electroformed at 60 °C in sucrose (20 mM) and diluted in equimolar solution of glucose (containing EhVps20 t at the specified concentration in the case of the lipid mixture with lower amount of cholesterol). The choice for working in low sugar concentration was set to avoid influence of gravity on the vesicle shape as well as softening effects of sugars.[83,106,107] After 5 min incubation, the vesicles were placed in a chamber made of two cover slips and a 2 mm-thick Teflon spacer, and observed under phase-contrast mode on a Zeiss Axio Observer D1 microscope using a 40× air objective. 3600 snapshots (per vesicle) were acquired with a digital camera (pco.edge, PCO AG, Kelheim, Germany) at frequency of 60 frames per second and image exposure time of 200 μs, at room temperature (~23 °C). The bending rigidity of vesicles in the absence and presence of EhVps20t (125 nM) was extracted. In each case, at least eight vesicles were examined.

Dynamic light scattering and zeta potential measurements

Large unilamellar vesicles (LUVs) were used to determine the zeta potential of the POPC:POPS (80:20) and POPC:POPS:Chol:PI(3)P (62:10:25:3) lipid mixtures. Both lipid compositions, with total lipid concentration of 0.75 mg/mL, were prepared from chloroform lipid stock solutions. The solvent was evaporated under a stream of N_2 and the lipid films were further dried under vacuum for 2 h to remove chloroform traces. The lipid films were hydrated in protein buffer (25 mM Tris, 150 mM NaCl, pH = 7.4) to a final concentration of 0.5 mM and gently stirred for 10 min. The obtained lipid suspensions were extruded 30 times through polycarbonate membranes with 100 nm pores (WHA70602501, Sigma Aldrich) using a LiposoFast pneumatic extruder (Avestin, Otawa, Canada). The size and the zeta potential of the LUVs were measured with a zetasizer Nano ZS (Malvern Instruments, Worcestershire, UK) equipped with a 4 mW HaNe laser (632.8 nm), a detector positioned at a scattering angle of 173° and a temperature controlled cuvette holder. Three dynamic light scattering (DLS) measurements consisting of 20 runs with duration of 10 s at 25 °C were performed. The obtained intensity size distributions exhibited a peak at 120 nm. For the zeta potential measurements, 750 μL of the samples were loaded in DST1060 folded capillary cells with integral gold electrodes (Malvern Instruments, Worcestershire, UK). Three measurements each consisting of 70 runs were performed for every sample at 25 °C. Zeta potential was deduced from the electrophoretic mobility, μ_e, data using the Smoluchowski and Hückel equation,[108] $\zeta = 3\mu_e\eta/[2\varepsilon\varepsilon_0 f(R/\lambda_D)]$ where η is the viscosity of the aqueous solution ε_0 and ε are the permittivity of free space and the relative permittivity of the medium, and $f(R/\lambda_D)$ is the Henry function. The latter depends of the vesicle radius R and the Debye length λ_D of the solution. For $1 < \lambda_D < 1000$, as for the samples used here (the radius of the LUVs is 60 nm as measured with DLS), a prefactor of $f\left(R/\lambda_D\right) = \frac{1}{6} log\left(R/\lambda_D\right) + 1$ was taken into account in the analysis, see.[109] The Debye length λ_D for the samples was extracted based on its measured conductivity using $\lambda_D = \sqrt{(\varepsilon\varepsilon_0 D)/K}$, where the D is the diffusion constant of water $D = 2.299 \times 10^{-9}$ m^2/s[110] and K is the solution conductivity which was measured $K = 2.87$ S/m. This yields for the Debye length $\lambda_D = 0.75$ nm. The respective zeta potentials of POPC:POPS (80:20) and POPC:POPS:Chol:PI(3)P (62:10:25:3) vesicles in the used buffer were measured to be −14 mV and −17 mV which are indistinguishable considering the instrument accuracy of ~5 mV.

Inflation/deflation experiments in the bulk

POPC:POPS:Chol:PI(3)P (62:10:25:3) GUVs were prepared by electroformation in a high osmolarity sucrose solution (~650 mOsm/Kg). Then, the GUVs were diluted 1:1 vol:vol in a 2-fold protein buffer (50 mM Tris pH = 7.4, 300 mM NaCl, adjusted to have 5% higher osmolarity to ensure excess membrane area for bud formation) and incubated with 125 nM of EhVps20t and 600 nM of EhVps32, leaving 5 min of incubation between each protein addition (mixture 1). Note that incubation of the vesicles in protein-free buffer

resulted in visibly fluctuating vesicles and occasional inward nanotubes with sub-optical thickness but never micron-sized buds; the vesicles were also deformed into oblates due to gravity. For the subsequent inflation/deflation steps, we used protein buffer (25 mM Tris pH = 7.4, 150 mM NaCl) with the appropriate amount of proteins and adjusted the osmolarity with sucrose to achieve the work conditions indicated in the main text. This was done in order to keep the salt and protein concentrations equal throughout the whole experiment. When ILVs were visible in the GUVs, mixture 1 was diluted 1:2 (vol:vol) with a hypotonic buffer solution (~450 mOsm/Kg) to obtain an inflation of ~20% and incubated the sample for 20 min to equilibrate (mixture 2). Afterward, the inflated GUVs of the mixture 2 were incubated 1:1 with a hyperosmotic buffer (~630 mOsm/Kg) to reach a deflation of ~10%. In all conditions, at least 30 vesicles were observed after each step.

Fluorescence recovery after photo bleaching (FRAP)

FRAP measurements were performed on intraluminal buds as well as on the GUV surface. Movement of the vesicles in the sample because of convection hindered the experiments. To minimize the GUV movement during the measurements the vesicles were immobilized in agarose following the methodology in.[111] Briefly, electroformed vesicles (grown in sucrose) were incubated with 125 nM EhVps20t and 300 nM OG-EhVps32 for 10 min 8 μL of the GUV-protein mixture were deposited on a cover glass (passivated with BSA) and immediately 2 μL 0.5% w/v preheated agarose solution diluted in the protein buffer were added. The solutions inside and outside the GUVs were osmotically balanced. Confocal microscopy images were recorded at 1000 Hz with a pinhole size of 1 Airy unit in bidirectional mode and with an image size of 512 x 512 pixels and at room temperature (23 °C). OG-EhVps32 was exited using the 488 nm line of the argon laser and the fluorescence signal was detected in the range 493–550 nm, while $DiIC_{18}$ was excited with the 561 nm laser line, and the fluorescence signal collected at 567–628 nm. Pre-bleaching, 10 frames at attenuated laser intensity (below 5%) were recorded. The photobleaching was performed for 505 ms (3 frames) at 100% laser intensity using a circular region of interest (ROI) of nominal radius r_n = 3.6 μm, and 3 μm in the case of intraluminal buds or the top of the GUVs, respectively. The post-bleach recovery images were then recorded at the initial attenuated laser intensity for 100 frames. The diffusion coefficient, D, from the FRAP recovery performed on the top of the GUV was extracted using $D = r_e^2 + r_n^2/8t_{1/2}$ where r_e and r_n are the effective and the nominal radii, respectively and $t_{1/2}$ is the half-time for the dye photorecovery.[112] Some of the bleached buds (roughly 70%) showed non-monotonous recovery curves, because the buds were diffusing and leaving the focal plane during the measurement; this could be also observed in the images acquired under phase-contrast imaging. Such recovery data were discarded to avoid contribution to the signal due to bud defocusing.

Measurement of the protein coverage at the vesicle membrane

GUVs composed by 80 mol % POPC, 20 mol % POPS and different concentrations of OG-DHPE (0.1, 0.25, 0.5 and 0.75 mol %) were generated by electroformation as detailed before. GUVs were observed with a Leica TCS SP5 confocal microscope. In order to calculate the absorption of EhVps20 t at the membrane, a calibration curve of the dye was generated. Following the procedure from,[65] we first checked that the intensity of the Oregon green 488-labelled protein (OG-EhVps20t) behaves linearly with the concentration of the fluorophores present in the sample. Thus, we measured the fluorescence intensity of different concentrations of the labeled protein using confocal microscopy while maintaining the same microscope settings and objective for the whole quantifications. Figure S3 shows the linear dependence of the intensity obtained from these experiments.

Next, for measuring the intensity at the level of the membrane, we used the "Radial Profile Extended Plugin" from Philippe Carl available in the ImageJ homepage. We prepared GUVs made of POPC:POPS (80:20) including various concentrations of the labeled lipid OG-DHPE (0.01, 0.025, 0.05 and 0.075 mol %) in the mixture. The radial intensity profile of the different GUVs was obtained at the equatorial plane. To avoid polarization issues resulting from the dye orientation with respect to the membrane, the intensity was radially averaged along the circular vesicle contour. An example of an intensity profile is shown in Figure S4. The integrated peak area is then taken as the intensity for the specific fluorophore concentration in the membrane. The scatter in the data obtained in Figure 2A in the main text results from the fact that we have analyzed vesicles of different sizes whereby out-of-focus fluorescence contributions vary. To use the obtained calibration curve in Figure 2A and deduce the amount of bound protein, we have divided this intensity value by a factor of 2 as to correspond to fluorescence from the outer vesicle leaflet (as is the case of adsorbing OG-labelled protein).

Finally, to calculate the adsorption of OG-EhVps20 t at the membrane of the GUVs, we took into consideration the signal from the unbound protein in the bulk solution and subtracted it. Figure S5 illustrates the procedure that we followed. We also considered possible differences in the quantum yield of the label OG when bound to both lipid and protein, see Figure S6A. Confocal images at identical settings of the microscope, same objective and identical height in the sample were recorded. The following solutions were images: i) a lipid mixture containing OG-DHPE in POPC:POPS (80:20) and ii) OG-EhVps20t in POPC:POPS (80:20). The bottom coverslip of the observation chamber was coated with 2% casein solution to avoid sticking of the protein to the glass and thus effectively lowering the concentration of the OG-EhVps20t. The objective was always kept at 20 μm above the glass to avoid possible signal contribution from the adsorbed casein. Three different ROI per image were analyzed using ImageJ. The size of the ROIs were the same for all images. Then the intensity values (i.e. the signal from the OG) were normalised to the amount of OG present in the corresponding sample. The data is displayed in Figure S6A. To correct for the different quantum yield, the ratio between the two different averaged intensity values was used. The protein coverage on vesicles prepared from POPC:POPS:Chol:PI(3)P (62:10:25:3) was found to be similar as expected from the comparable surface charge, see Figure S6B.

Micropipette aspiration of GUVs

Micropipettes were pulled from borosilicate capillaries (1B100-4, World Precision Instruments Inc.) with a pipette puller (Sutter Instruments, Novato, CA) and then shaped with a microforge (Narishige, Tokyo, Japan). The inner pipette diameter varied in the range of 10–15 μm. The pipette tips were incubated in protein buffer (25 mM Tris, 150 mM NaCl, pH = 7.4), containing 1% BSA to prevent adhesion of the vesicle membrane to the pipette. After the incubation, the micropipette was rinsed with the protein buffer to remove the free BSA. Aspiration of GUVs was performed in a homemade experimental chamber with volume of 0.5 mL. The chamber was built from two parallel glass coverslips separated by a Teflon spacer with opening from one side for inserting the micropipette. To prevent vesicle adhesion, the glasses were passivated with 1% BSA solution prior to chamber assembly. The vesicles were observed on a Leica TCS SP5 confocal microscope (Mannheim, Germany), equipped with 40× objective. $DiIC_{18}$ was excited with a diode-pumped solid-state laser 561 nm laser and the fluorescence signal was collected in the ranges of 580–700 nm. The micropipette was operated using a three-dimensional micromanipulator system (Sutter Instruments, Novato, CA) mounted on the microscope. The aspiration pressure in the micropipette was controlled by changing the height of a water reservoir mounted on a linear translational stage (M-531.PD; Physik Instrumente Germany). Equilibrium height of the water reservoir corresponding to zero pressure across the pipette tip was set prior to each measurement.

The membrane tension was assessed as

$$\Sigma = \frac{\Delta P R_p}{2(1 - R_p/R_{ve})}$$

where ΔP is the suction pressure, R_{ve} and R_p are respectively the radii of the spherical vesicle and the micropipette. Since the ILVs are connected via a narrow neck to the mother vesicle the upper limit of the spontaneous curvature m can be estimated from the neck closure condition $m \leq M_{ne} + \frac{1}{2R_W} = \frac{1}{2}(1/R_{ve} - 1/R_{ILVs}) + \frac{1}{2R_W}$, where R_{ILVs} is the average radius of all ILVs and $R_W = (2\kappa/|W|)^{1/2}$ is the adhesion length with the adhesion strength $|W|$ between the membrane and the protein assembly.[70] The estimates for the spontaneous curvature m in the main text have been obtained by omitting the term $\frac{1}{2R_W}$ reflecting our ignorance about the adhesion strength $|W|$ The spontaneous tension is then $\sigma_m = 2\kappa m^2$, where κ is the bending rigidity of the membrane. This estimate is valid for homogeneous membranes (same κ and m for vesicle and buds). The area expansion ($\Delta A/A_0$) was calculated using Equation 46 from.[113]

QUANTIFICATION AND STATISTICAL ANALYSIS

To analyze the obtained data, several normality tests were performed, namely Shapiro-Wilk, Anderson-Darling, D'Agostino-K and Chen-Shapiro and then, a two-sample test of variance was executed. Finally, two-sample t-test or one-way ANOVA analysis were performed. All tests were accomplished at the 0.05 level (cut-off for significance).

iScience, Volume *26*

Supplemental information

Stepwise remodeling and subcompartment formation in individual vesicles by three ESCRT-III proteins

Yunuen Avalos-Padilla, Vasil N. Georgiev, Eleanor Ewins, Tom Robinson, Esther Orozco, Reinhard Lipowsky, and Rumiana Dimova

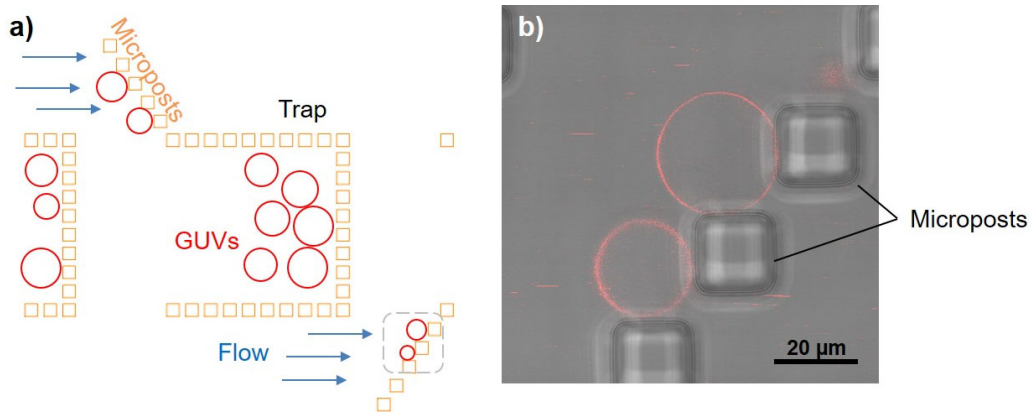

Figure S1. Vesicle trapping in a microfluidic device, related to Figure 1. (a) A sketch of part of the microfluidic chip reported previously [S1], showing a trap and the microposts by which individual vesicles can be stopped and monitored. (b) An overlay of confocal and phase-contrast image showing two vesicles trapped by the posts in a microfluidic device (as illustrated by the dashed-line region indicated in panel a). The flow direction of introduced solution is from the left.

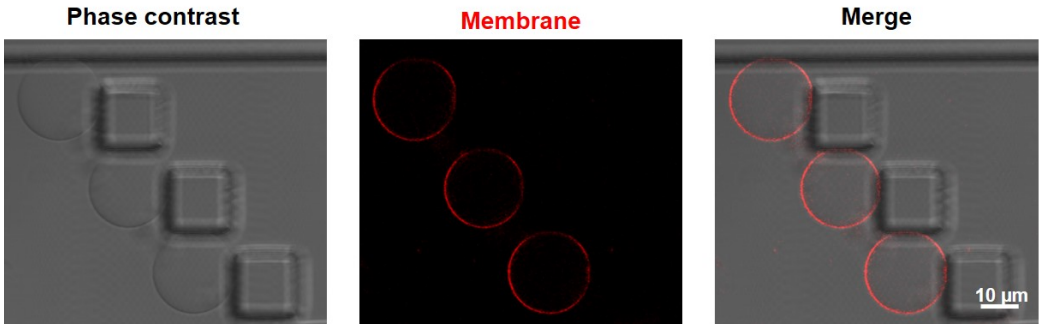

Figure S2. Buffer flushing and incubation of GUVs does not result in ILV formation, related to Figure 1. POPC:POPS:Chol:PI(3)P (62:10:25:3) GUVs were incubated with equivalent protein-free buffer (25 mM Tris, 150 mM NaCl, pH = 7.4) volumes as in Figure 1. Images show 3 GUVs after six rounds of buffer exchange, similar to the conditions shown in Figure 1.

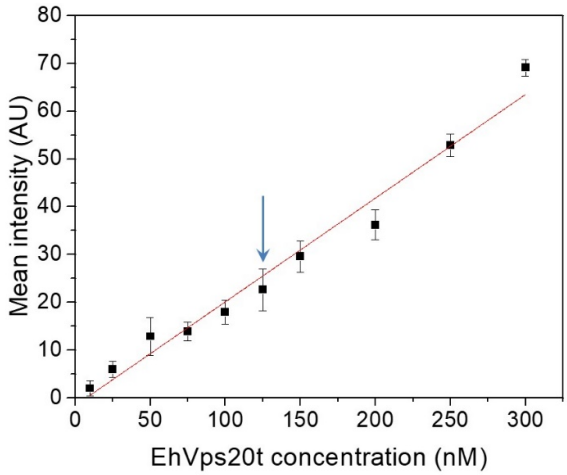

Figure S3. Linear dependence of the bulk fluorescence intensity of OG-EhVps20t, related to Figure 2. OG-EhVps20t mixed with unlabelled EhVps20t (1:4, v:v) dissolved in 25 mM Tris, 150 mM NaCl, pH = 7.4 at room temperature. Arrow points to the typical working concentration. The red line is a linear fit. The error bars represent the standard deviations of 20 GUVs observed for each condition.

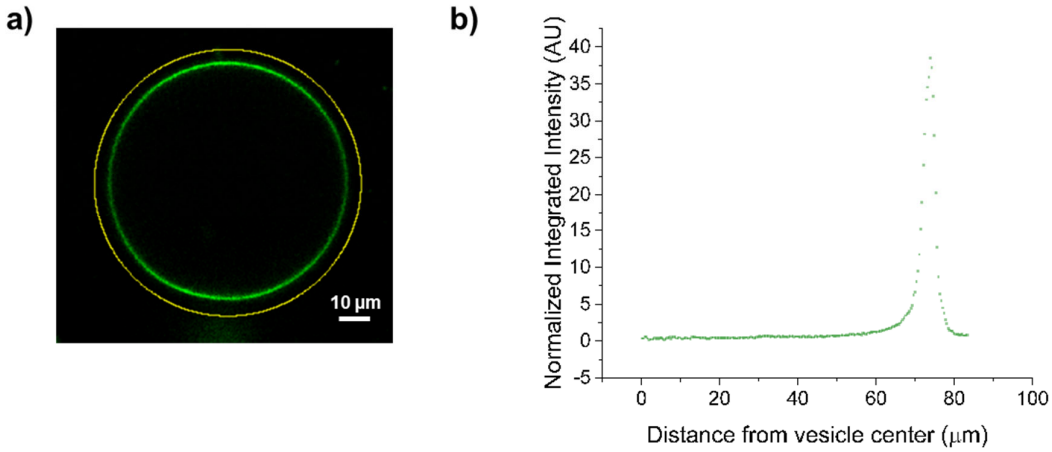

Figure S4. Standard curve generation, related to Figure 2. (a) Representative confocal image of a vesicle labelled with OG-DHPE used for the standard curve generation; the polarization effect is visible from the angular dependence of the florescence. (b) Typical intensity radial profile. The value of intensity was obtained by measurement of the area under the curve generated in the plot.

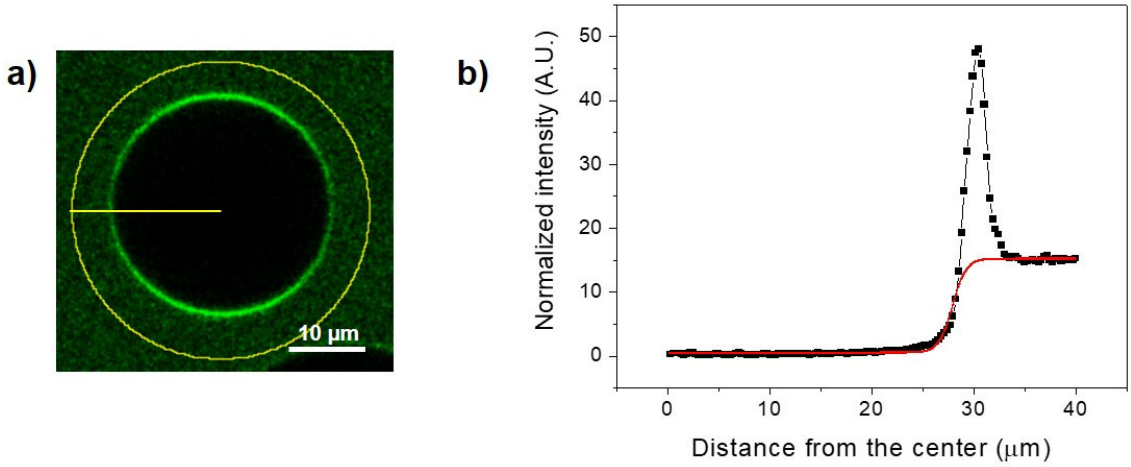

Figure S5. OG-EhVps20t coverage measurement, related to Figure 2. (a) Typical confocal image of a GUV used for measuring the coverage concentration of OG-EhVps20t at the membrane. (b) Radial intensity profile (black squares) and subtracted intensity of the non-adsorbed protein in the bulk (red curve).

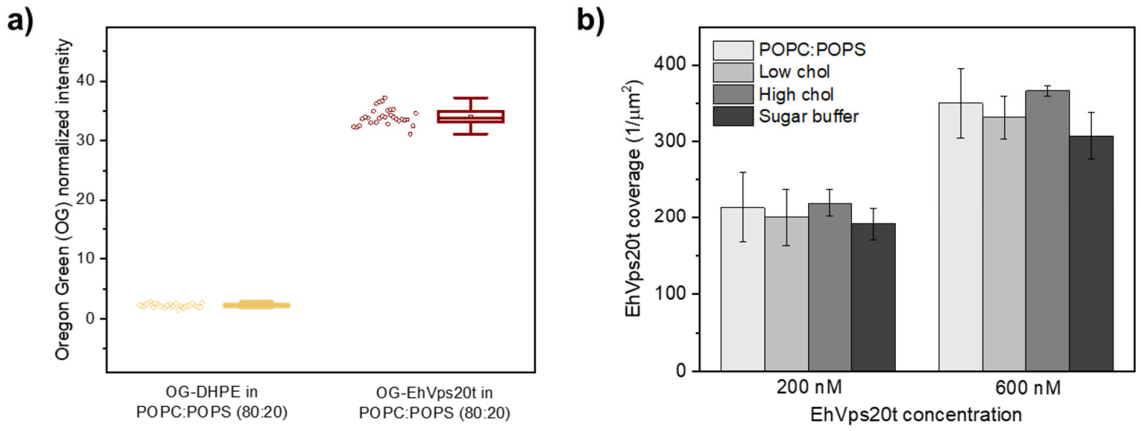

Figure S6. Assessing the EhVps20t coverage from intensity measurements, related to Figure 2. (a) To account for the different quantum yield of OG in the labeled lipid and the protein, the intensity of lipid solutions and that of the protein in the presence of the lipid solutions at identical settings of the microscope were evaluated (see STAR Methods). Each symbol (on the left side of the boxes) corresponds to an individual measurement. The samples were diluted in the normal protein buffer (25 mM Tris, 150 mM NaCl, pH = 7.4). The signal is normalized by the concentration of OG. (b) Protein coverage of EhVps20t at two different concentrations of the protein present in the bulk. In order from left to right, different types of conditions were tested (1) POPC:POPS (80:20) GUVs, (2) POPC:POPS:Chol:PI(3)P (62:10:25:3) GUVs (Low chol) and (3) POPC:POPS:Chol:PI(3)P (6:10:35:3) GUVs (High chol), incubated in the normal protein buffer (25 mM Tris, 150 mM NaCl, pH = 7.4). The darker bar, represent results from POPC:POPS:Chol:PI(3)P (62:10:25:3) GUVs incubated in sugar buffer (600 mM Sucrose). At least twenty vesicles were measured for each condition, standard errors are shown for each bar.

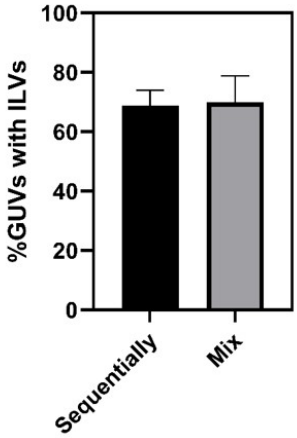

Figure S7. Effect on ILV formation by protein addition approach – sequentially or premixed, related to Figure 3**.** POPC:POPS:Chol:PI(3)P (62:10:25:3) GUVs were incubated with 125 nM of EhVps20t, 600 nM of EhVps32 and 300 nM EhVps24, either sequentially leaving 5 min of incubation between each protein addition or together in a mix leaving 15 min incubation at the end. Data represent the mean and standard error of three independent experiments where 30 GUVs of each replicate were screened.

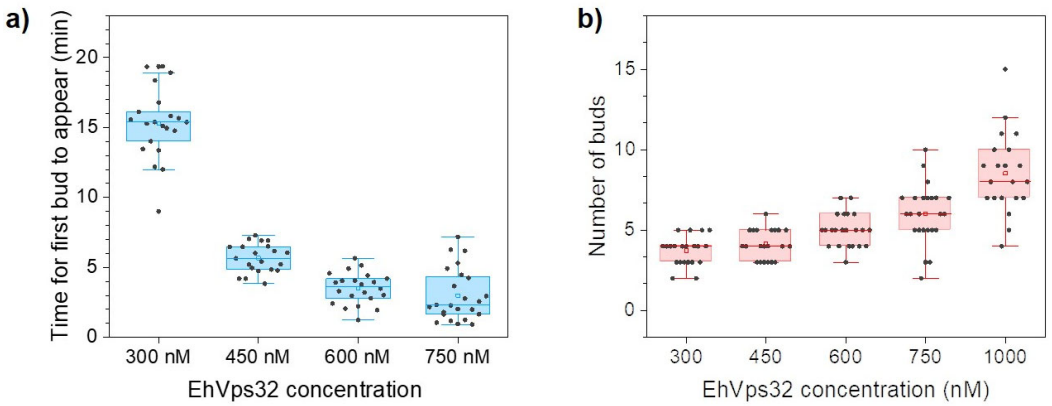

Figure S8. Kinetics of bud formation regulated by EhVps32 concentration, related to Figure 4. POPC:POPS:Chol:PI(3)P (62:10:25:3) GUVs were incubated with 125 nM of EhVps20t for 5 min followed by different concentrations of EhVps32 as shown in the x-axis. At least 10 vesicles of three independent preparations were followed over time in a microfluidic device and (a) the time that took for the first bud to be observed is plotted. At higher concentrations of EhVps32, namely 1000 nM, the process was faster than 1 minute and the exact time frames could not be determined because of difficulties in experimental handling. (b) Total number of buds detected in each GUV after 30 min of incubation with EhVps32. Black data points show the single measurements for each condition. Boxes show the range from 25-75% of data and the median line.

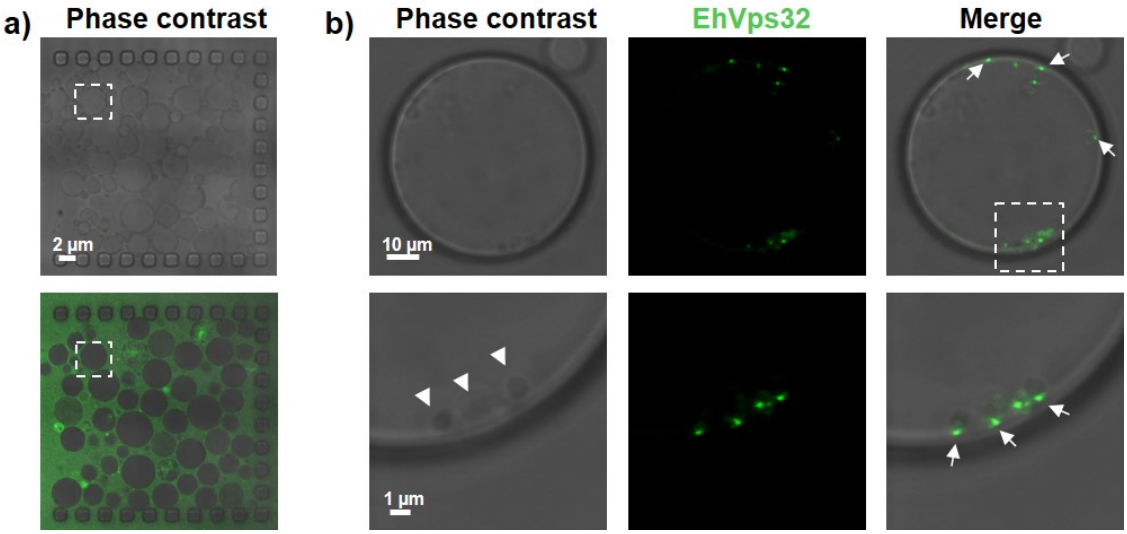

Figure S9. EhVps32–enriched domain formation in GUVs, related to Figure 4. (a) POPC:POPS:Chol:PI(3)P (62:10:25:3) GUVs were loaded on a microfluidic chamber at a flow rate of 10 µl/min. Then 125 nM of EhVps20t and 300 nM of EhVps32 (20% of EhVps32 was labelled) were subsequently flushed at a constant rate of 0.1 µl/min. (b) Close-up views of the vesicle in the dashed region in (a) after the excess of proteins was washed away, showing protein-domain formation (arrows) in the site where buds (arrowheads in phase-contrast image) are generated.

	EhVps32 (nM)		
EhVps20t (nM)	**300**	**600**	**1000**
125	2.46 ± 0.64^{a}	1.29 ± 0.28^{b}	1.05 ± 0.25^{c}
300	3.51 ± 0.56^{d}	3.08 ± 0.49^{e}	2.35 ± 0.40^{a}
600	4.11 ± 0.31^{f}	3.70 ± 0.64^{d}	2.53 ± 0.44^{a}

Table S1. Statistical analysis of the data in Figure 5 in the main text. Data are means ± SE of ILVs diameter measured in at least 20 GUVs. Significant differences ($p < 0.05$, Tukey's test) calculated using one-way ANOVA are denoted by different letters: shared letters represent no statistically significant difference as evaluated with the SPSS statistics software for Windows v17.0 (Chicago: SPSS Inc.).

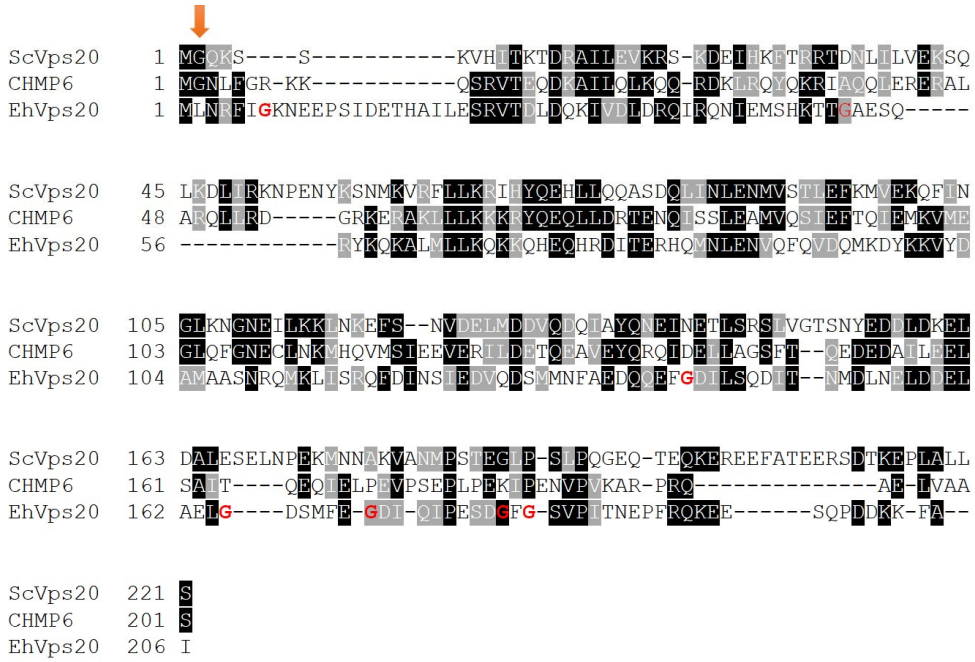

Figure S10. Blast analysis of EhVps20 with its human and yeast homologues, related to Figure 5. EhVps20 lacks the glycine residue in its N-terminal necessary for protein myristoylation. Multiple sequence alignment for Vps20-homologues in yeast (ScVps20), human (CHMP6) and *E. histolytica* (EhVps20). Glycine residues present in EhVps20 are displayed in red. Arrow indicates the N-terminal glycine necessary for protein myristoylation. Sequence alignments were performed with Clustal Omega and edited in the BoxShade server (https://embnet.vital-it.ch/software/BOX_form.html).

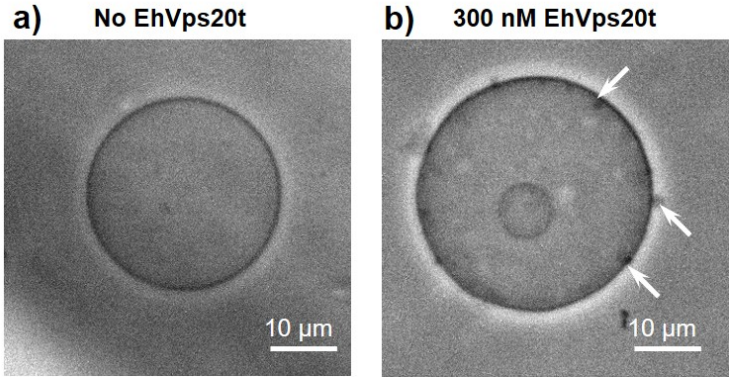

Figure S11. EhVps20t clusters in the membrane of GUVs at high protein concentrations, related to Figure 5. Electroformed POPC:POPS:Chol:PI(3)P (62:10:25:3) GUVs incubated in (a) a isoosmolar sucrose buffer (no EhVps20t) or (b) 300 nM of EhVps20t, observed under phase contrast. Arrows show protein clusters at the membrane.

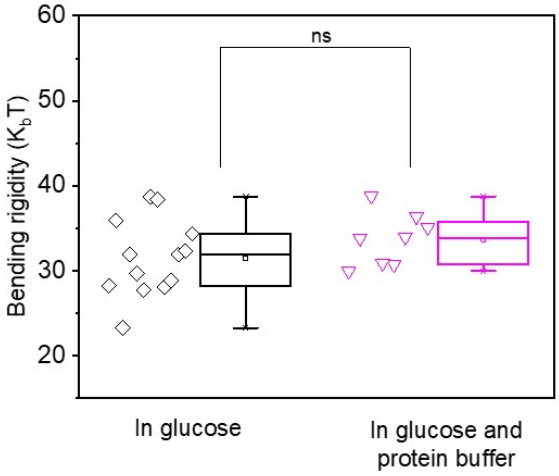

Figure S12. Bending rigidity of protein-free membranes, related to Figure 5. The vesicles were formed of POPC:POPS:Chol:PI(3)P (62:10:25:3) in 20 mOsm/Kg sucrose solution. The GUVs for the data set indicated by the black diamonds (the same data as "Low Chol" in Figure 5c in the main text) were diluted in isotonic glucose solution, while the vesicles used for the data in magenta triangles were diluted in a solution containing protein buffer and glucose. The latter solution represents the scenario when 125 nm EhVps20t was used (see Figure 5c in the main text).

Reference

1. Yandrapalli, N., and Robinson, T. (2019). Ultra-high capacity microfluidic trapping of giant vesicles for high-throughput membrane studies. Lab Chip *19*, 626-633.